Transfer-Power Measurement Using a Non-Contact Method for Fair and Accurate Metering of Wireless Power Transfer in Electric Vehicles

Sung Yul Chu, *Student Member, IEEE*, Xiaofan Cui, *Student Member, IEEE*, Xin Zan, *Student Member, IEEE*, and Al-Thaddeus Avestruz, *Member, IEEE*

***Abstract*—Wireless power transfer (WPT) is emerging as the preeminent way to charge electric vehicles, but there appears to be no fair way to measure the power transfer. In this article, *Faraday coil transfer-power measurement* (FC-TPM) is presented. FC-TPM employs non-contact, open-circuited sense coils to measure the electromagnetic field from WPT and calculates the real power propagating through the air gap between the transmitter and receiver coils. What is measured is the real electromagnetic power, representing the pure dispensation of energy that unambiguously demarcates the losses on either side. FC-TPM was demonstrated to be 0.1% accurate in hardware over an Rx coil misalignment of up to 10 cm using a 1-kW WPT system. Fair metering incentivizes businesses and individuals to make choices that conserve energy and advance technology by providing more information and by properly assigning the financial loss. This article is accompanied by a video highlighting the essential contributions of this article.**

***Index Terms*—Charging, diagnostics, electric vehicles (EVs), electromagnetic modeling, energy metering, Faraday coil, measurement, metering, non-contact sensors, power measurement, power metering, power transfer, Poynting vector, sense coil, transfer-power, wireless power transfer (WPT).**

I. Introduction

TRUST in technology is essential for adoption. Our society accepts what is fair, safe, and robust to use, where accurate measurement provides the discernment of those values. This article presents a fair and accurate measurement method for wireless power transfer (WPT).

WPT is a fast-growing technology for charging electric vehicles (EVs) [1]–[6] with continuing achievements in maximum power transfer and high efficiency [7]–[12] along with effective coil design [13]–[15] and electromagnetic exposure safety [9], [16], [17].

Fairness in metering WPT has an integral significance to providers and consumers of energy as an arbiter in their competing financial interests. By 2030, EVs will consume over 1000 terawatt–hours of electricity every year worldwide; even a 1% misrepresentation in metering will cost energy consumers and providers over $ 1 billion[1] [18]–[21].

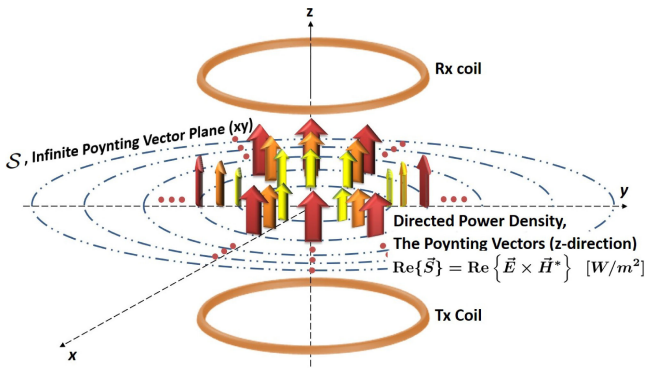

Fig. 1. Poynting vector is the directed power density. Transfer power is equivalent to the surface integration of the components of the Poynting vectors that are normal to a surface S between the transmitter (Tx) and receiver (Rx) coils.

For fairness, the cost of lost energy must be appropriately assigned among the stakeholders. Transmitter losses must be disaggregated from receiver losses for the equitable metering of WPT. Energy station owners and EV owners will then be individually motivated to improve their efficiency and hence reduce their financial losses.

The proper demarcation line for the "point of sale" in wireless charging had been posited to be physically between the transmitter (Tx) and vehicle receiver (Rx) coil by [22].[2] Transfer-power (P_{Transfer}) is the missing link. It is the real power through the air gap, purely dispensed from the Tx coil to the Rx coil. This real power can be represented electromagnetically through the Poynting vector illustrated in Fig. 1.

At first glance, there appeared to be no direct way to measure the quantity of power transfer; rather, what had been currently available were only the voltages and currents at the Tx and Rx electrical terminals with which to calculate the Tx input

Manuscript received January 7, 2021; revised April 30, 2021; accepted August 3, 2021. Date of publication August 18, 2021; date of current version October 15, 2021. Recommended for publication by Associate Editor K. Madawala. *(Corresponding author: Sung Yul Chu.)*

The authors are with the Electrical and Computer Engineering, University of Michigan, Ann Arbor, MI 48109-1382 USA (e-mail: sungyul@umich.edu; cuixf@umich.edu; xinzan@umich.edu; avestruz@umich.edu).

This article has supplementary material provided by the authors and color versions of one or more figures available at https://doi.org/10.1109/TPEL.2021.3105689.

Digital Object Identifier 10.1109/TPEL.2021.3105689

[1]Based on EV projections: 1) 250 million EVs by 2030 [18]; 2) 4500 kWh/year/EV [19]; 3) $0.1/kWh, the 10-years average price of electricity to ultimate customers in the transportation category [20].

[2]Subgroup in the U.S National Work Group on Measuring Systems for Electric Vehicle Fueling and Submetering, sponsored by the National Institute of Standards and Technology (NIST).

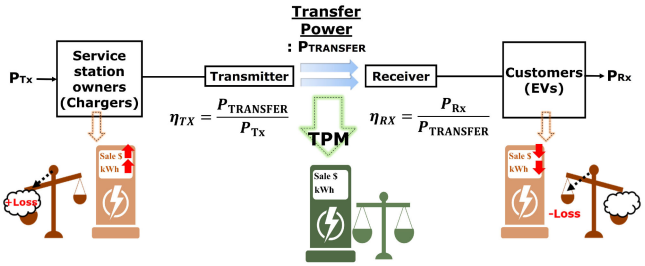

Fig. 2. Transfer-power measurement results in fair metering and accurate diagnostics by disaggregating the efficiency of the transmitter (Tx) and receiver (Rx).

Fig. 3. U.S. Weights and Measure Program qualifies secured gas pump metering (left) with a seal (right). [Photo (left): Weights and Measures, Maryland Department of Agriculture].

(P_{Tx}) and Rx output (P_{Rx}) power, which had been performed to varying degrees of accuracy and robustness in [23] and [24]. The shortcoming of these methods is that Tx input and Rx output power necessarily incorporate aggregated losses from both sides, including those from winding resistance and eddy currents [25], [26].

Except for the unlikely case that the losses are symmetric in Tx and Rx, the correct attribution of power inefficiency is not possible. Fig. 2 illustrates the conundrum: Input or output power measured at the Tx or Rx electrical terminal imposes the cost of the aggregated losses to one side or the other unilaterally; for example, if power is measured at the Tx terminal (P_{Tx}), metering adds Tx losses to the evaluation of transferred power, which ought to have been excluded in pricing, and thus, customers are overcharged. Likewise, metering at the customer (Rx) terminal (P_{Rx}) subtracts Rx losses from the evaluation of transferred power and hence represents an undercharge. These inequities are exacerbated in systems, where low efficiency from cost-cutting in design, production, installation, or maintenance is incentivized without proper metering, with another potential for abuse when there is physical access to the measurement terminals. Even if power efficiency is legislated, a robust way to validate disaggregated efficiencies is still needed.

These flaws can be overcome by measuring the transfer-power through the air gap between the Tx and Rx coils, as shown in Fig. 2. Not only will this provide fair metering, but will also disaggregate individual Tx and Rx efficiencies, $P_{\text{Transfer}}/P_{\text{Tx}}$ and $P_{\text{Rx}}/P_{\text{Transfer}}$, respectively. As a diagnostic, it can financially incentivize the decisions and behaviors of providers and customers.

The subject of this article, *Faraday coil transfer-power measurement* (FC-TPM), originated in the following conference papers [27], [28], which to our knowledge is a first among methods in directly metering wireless charging of EVs. This journal article significantly expands on the original conference papers by the following: 1) providing a direct connection to the Poynting vector; 2) a thorough decomposition and analysis of the power balance that includes eddy current losses from cross-coupled magnetic fields; 3) FEM analyses for losses; 4) performance analysis of coplanar sense coils; and 5) verification on kilowatt-level WPT hardware.

FC-TPM employs non-contact open-circuited sense coils that are electromagnetically coupled to the Tx and Rx coils from which transfer-power is reconstructed. These sense coil voltages directly map to the Poynting vector, which is the directed power density, as shown in Fig. 1. FC-TPM is analogous to *trusted third party* gasoline fuel pump metering today from an arbitration perspective with inspection performed by an unbiased third party: for example, the Michigan Department of Agriculture's *Weights and Measures Program* as illustrated in Fig. 3.

The rest of article is organized as follows. Section II defines the transfer-power from the Poynting vector and presents a formulation based on a transformer model. Section III presents the transfer-power in lossy WPT coils from a winding loss model. Section IV presents FC-TPM: We derive the mapping of the sense coil voltages to the Poynting vector to validate FC-TPM as a fundamental measurement of WPT's real power flow and also show why employing multiple sense coil voltages makes FC-TPM accurate over misalignment between the Rx coil and Tx coil. Section V discusses how FC-TPM sense coils can be designed to be both physically and electromagnetically unobtrusive. Section VI demonstrates accurate FC-TPM in hardware over a standardized Rx coil misalignment of up to 10 cm with a 1 kW WPT system. Finally, Section VII is a summary of the main contributions of this article towards future research.

II. Transfer-Power Defined From the Poynting Vector in Wireless Power Transfer

In WPT, we define *transfer-power* to be the real power propagated from a transmitter (Tx) coil to a receiver (Rx) coil through the intervening space. In this section, the formulation for transfer-power is derived through both the Poynting vector and a transformer model; additionally, we show how these two formulations are equivalent and directly map to each other.

A. Transfer-Power From the Poynting Vector

P_{Transfer} or transfer-power can be defined from the Poynting vector, which is the directed electromagnetic power density and is determined by the cross product of the electric field $\vec{E}$ with the magnetic field $\vec{H}$ [29]. The average power p_{avg}, which is the real transfer-power, can then be obtained by a surface integral of the real part of the time-averaged complex Poynting vector $\vec{S}$

$$P_{\text{Transfer}} \triangleq p_{\text{avg}} = \iint_{\mathcal{S}} \text{Re}\{\vec{S}\} \cdot d\vec{s} \tag{1}$$

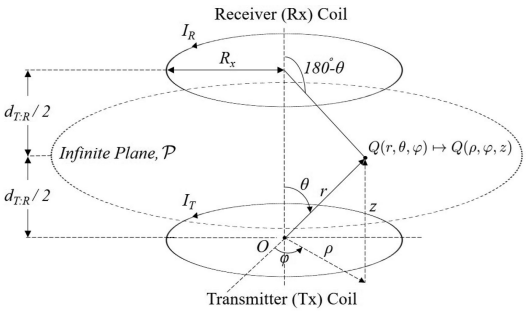

Fig. 4. Fields from the Tx and Rx coil currents are modeled as magnetic dipoles. The magnetic and electric fields are calculated and then transformed from spherical to cylindrical coordinates to derive the Poynting vector in the WPT system.

where

$$\vec{S} = \vec{E} \times \vec{H}^*. \tag{2}$$

Note that, $\vec{E}$ and $\vec{H}$ are the phasors of time-harmonic fields whose magnitude is the rms value. $\mathrm{Re}\{\cdot\}$ indicates the real part and the asterisk (*) indicates the complex conjugate.

The Tx and Rx coils can be approximated as circular current loops whose basic physics can be illustrated by magnetic dipoles [30], as shown in Fig. 4 to derive the Poynting vector. The radii R_x of the Tx and Rx current loops are identical and assumed to be much smaller than the distance between the two coils $d_{T:R}$ ($R_x \ll d_{T:R}$). The Poynting vector through the point $Q : (r, \theta, \varphi)$ in spherical coordinates is analyzed on the infinite plane $\mathcal{P}$, which is located at $z = d_{T:R}/2$ between the Tx and Rx coil, as shown in Fig. 4, where the magnetic field $\vec{H}$ and electric field $\vec{E}$ created by the magnetic dipoles were formulated in [30] and [31] in spherical coordinates. However, the Poynting vector and the resulting average power calculation can be represented more simply in cylindrical coordinates; the Poynting vector is derived from $\vec{E}$ and $\vec{H}$

$$\vec{E} = -\,\hat{\varphi}\, j\omega \frac{\mu_0 A}{4\pi r^2} \sin\theta\, (I_T + I_R) \tag{3}$$

$$\begin{aligned} \vec{H} = &\ \hat{\rho}\, \frac{3A}{8\pi r^3} \sin 2\theta\, (I_T - I_R) \\ &+\ \hat{z}\, \frac{A}{4\pi r^3}(3\cos^2\theta - 1)(I_T + I_R) \end{aligned} \tag{4}$$

where $A = \pi R_x^2$ is the Tx and Rx loop area, and I_T and I_R are the corresponding currents. Note that in cylindrical coordinates (ρ, φ, z)

$$r = \sqrt{\rho^2 + z^2}$$

$$\theta = \cos^{-1} \frac{z}{\sqrt{\rho^2 + z^2}}.$$

The real part of the time-averaged complex Poynting vector $\vec{S}$ is then

$$\begin{aligned} \mathrm{Re}\{\vec{S}\} &= \mathrm{Re}\{S_z\} \\ &= \hat{z}\, \frac{3\mu_0 A^2}{16\pi^2 r^5} \sin 2\theta \sin\theta\ \mathrm{Re}\{j\omega I_R I_T^*\}. \end{aligned} \tag{5}$$

Note that only the $\hat{z}$ component of the Poynting vector contributes to the real power transfer, where both the Tx and Rx coil currents I_T, I_R determine the magnitude and direction of the Poynting vector. Fig. 5 shows the time-averaged Poynting vector field, simulated by the finite element method (FEM) in COMSOL; power is transferred from the Tx coil to the Rx coil when the Tx coil current leads the Rx coil current (i.e., the Tx and Rx coil current phase difference is positive, $\theta_T - \theta_R > 0$). Particularly, there is maximum power transfer when the phase difference is 90°.

The transfer-power P_{Transfer} is the average power, which is calculated from (1), applying the surface integral to (5) over the infinite plane $\mathcal{P}$

$$P_{\text{Transfer}} = p_{\text{avg}} \tag{6}$$

$$= \mathrm{Re}\left\{ j\omega \underbrace{\frac{\mu_0 A^2}{2\pi {d_{T:R}}^3}}_{\text{Geometric Factor}} I_R I_T^* \right\}. \tag{7}$$

P_{Transfer}, the real power leaving the transmitter, is the real part of the product of the complex conjugate of the Tx coil current I_T^* and induced voltage $j\omega M_{R:T} I_R$ (from the Rx coil current), where the geometric factor is the mutual inductance $M_{R:T}$ from the Rx to the Tx coil, which also appears in the transformer model.

B. Transfer-Power in the Transformer Model

The Poynting vector illustrates how WPT operates. In practice, directly working with the Poynting vector is cumbersome; a transformer model is both elucidating and useful for the analysis and design of WPT.

Transfer-power can be formulated through a transformer model where losses are treated extrinsically. When a Tx and Rx coil pair are magnetically coupled through an air core, as shown in Fig. 6 and when there are no winding and eddy current losses, the Tx and Rx coil voltages (V_T and V_R) are

$$V_T = j\omega L_T I_T + j\omega M_{R:T} I_R \tag{8}$$

$$V_R = j\omega L_R I_R + j\omega M_{T:R} I_T \tag{9}$$

where L_T and L_R are the self-inductances of each coil; $M_{X:Y}$ is the mutual inductance from coil X to coil Y; ω is the angular frequency; and $\{V_X, I_X\}$ are the phasors whose magnitude is the rms value. Note that $M_{R:T} = M_{T:R}$ because of reciprocity.

In this article, the subscripts attribute each variable to a particular coil: T (Transmitter), R (Receiver), natural numbers $1, 2, \ldots$ (sense coils); colons $(x : y)$ indicate a parameter relationship from coil x to coil y.

In a WPT system with lossless coils,[3] the transfer power is equal to the real power at the coil terminals. The real power at the terminals of the Tx coil in this case is

$$P_{\text{Transfer}} = \mathrm{Re}\{V_T I_T^*\} \tag{10}$$

$$= \underbrace{\mathrm{Re}\{j\omega L_T I_T I_T^*\}}_{\text{Zero}} + \underbrace{\mathrm{Re}\{j\omega M_{R:T} I_R I_T^*\}}_{\text{Transfer-power}} \tag{11}$$

$$= \mathrm{Re}\{j\omega M_{R:T} I_R I_T^*\}. \tag{12}$$

[3]Section III elaborates on the transformer model with winding losses.

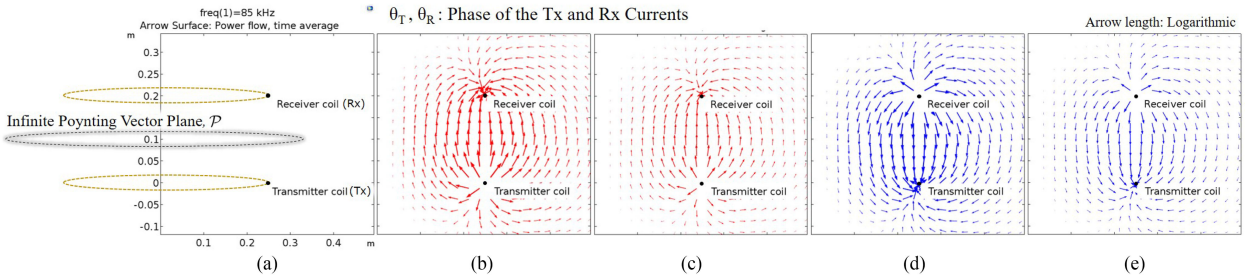

Fig. 5. Time-averaged Poynting vector field [arrows] is plotted from 2-D finite element method (FEM) simulations in COMSOL. The magnitude and direction of the power flow in WPT are represented by the Poynting vectors, which vary according to the Tx and Rx coil current phase differences ($\theta_T - \theta_R$). (a) $\theta_T = \theta_R$: There is no power transfer when the two coil currents are in phase. (b) $\theta_T - \theta_R$ =90°: Maximum power transfer from the Tx to the Rx when the Tx current leads the Rx current by 90°. (c) $\theta_T - \theta_R = 45°$: Real power is transferred from the Tx coil to the Rx coil when the Tx current leads the Rx current. (d) $\theta_T - \theta_R = -90°$: Maximum power transfer from the Rx to the Tx when the Rx current leads the Tx current by 90°. (e) $\theta_T - \theta_R = -45°$: Real power is transferred from the Rx coil to the Tx coil when the Rx current leads the Tx current.

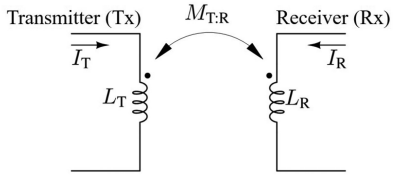

Fig. 6. Equivalent transformer circuit model for WPT.

Note that the combination of the incident magnetic field from the Tx coil current I_T and the reflected electric field from the induced voltage $j\omega M_{R:T} I_R$ from the Rx coil current I_R comprises transfer-power [30], [32]. The geometric factor in (7) is the mutual inductance $M_{R:T}$. The transfer-power can also be similarly derived from the Rx side as $\mathrm{Re}\{j\omega M_{T:R} I_T I_R^*\}$, which results in a negative value of P_{Transfer}, indicating that power is consumed by Rx.

III. Transfer-Power in Lossy Wireless Power Transfer Coils: Winding Loss Breakdown

The principal transfer-power, which we denote $P_{\text{Tx:Rx}}$, corresponds to the directed real power from the terminal currents described in Section II. However, for metering, principal transfer-power may not offer a complete description of transfer-power when cross-coupled loss mechanisms are significant.

Winding losses decompose into ohmic and eddy current losses, which we derive in this section. These losses manifest as heat dissipation in either the Tx or Rx coil, which is formulated from the coil (Tx or Rx) currents. Assignment of losses based on heat dissipation is consistent with the Poynting vector definition of transfer-power, which is the power flow through the intervening space between the Tx and Rx coils. Transfer-power is saliently different from the black box notion of input and output electrical terminal power.

Fair metering using transfer-power means that costs for power losses are imposed on the transmitter (service station owner) and the receiver (EVs owner) equitably based on the amount of the each side's physical power dissipation, which manifests as heating. This heat dissipation-based demarcation of the loss penalizes stakeholders who use inferior quality coils, power electronics, or other system components that cause loss. In other words, fair metering motivates providers and customers to advance their system (e.g., by using better litz wire or winding methods) to reduce losses.

A. Winding Losses in the WPT Coils

1) Input and Output Terminal Power: The input power P_{Tx} and output power P_{Rx} that are measured at the coils' electrical terminals are

$$P_{\text{Tx}} = \mathrm{Re}\{V_T I_T^*\} \tag{13}$$

$$P_{\text{Rx}} = \mathrm{Re}\{V_R I_R^*\} \tag{14}$$

where

V_T, V_R : Respective Tx, Rx coil terminal voltage

I_T, I_R : Respective Tx, Rx coil current.

The terminal voltage contains not only the induced coil voltages, represented by (8) and (9) but also the voltage drops that are related to winding losses, as shown in (89) and (90) in Appendix A. From the perspective of power conservation,[4] the difference between the Tx coil input power and the Rx coil output power is the aggregate power loss within both the Tx and Rx coils.

2) Winding Losses: The main purpose of our winding loss derivation and ensuing loss breakdown is to identify the source of each loss and to clarify where each loss is dissipated. This is especially important for WPT metering in that the Tx and Rx coils are magnetically coupled, where each coil's current and hence magnetic field can generate a loss in the other's coil.

Using a winding loss model[5] where eddy currents can be represented by an additional winding on a transformer, we can further show that the measurement of transfer-power disaggregates the losses between the Tx and Rx coils properly in contrast to the input and output terminal power, which lump both losses.

We decompose the winding losses into (i) ohmic losses due to ac and dc winding resistance and (ii) eddy current loss, which is the loss from eddy currents within a coil due to the external proximity effect, where the opposing coil generates an external magnetic field: For example, the external proximity effect loss in

[4]If the power is transferred from Tx to Rx, P_{Tx} can be considered positive for power generated and P_{Rx} negative for power consumed, without loss of generality.

[5]Derived in Appendix A.

the Rx coil due to the Tx coil current and resulting magnetic field. We refer to this external proximity effect loss as *eddy current loss* in this article.

Winding losses can be represented by the source currents

$$P_{\text{W,Tx}} = \text{Re}\left\{I_T^* I_T + \gamma_R I_T^* I_R\right\} R_T + \text{Re}\left\{I_T^* I_T\right\} R_{T:r} \quad (15)$$

$$P_{\text{W,Rx}} = \text{Re}\left\{I_R^* I_R + \gamma_T I_R^* I_T\right\} R_R + \text{Re}\left\{I_R^* I_R\right\} R_{R:t}\,. \quad (16)$$

$P_{\text{W,Tx}}$ represents the Tx winding loss, measured at the Tx coil terminal as a part of the input power; R_T is the effective winding resistance, which is frequency-dependent and accounts for the skin and internal proximity effects when there is no external field. The discussion of γ_R is identical to that of γ_T because the transmitter and receiver can be interchanged [for example, (15) and (16) are symmetric in the sense that R can replace T in the subscripts or vice versa to obtain the other equation, hence also reflecting the symmetry of the physics]. γ_R encapsulates the effect of geometry in how the external field from the Rx coil affects the current density distribution in the Tx windings. The external field can reinforce or weaken the self-field depending on its magnitude and relative phase, which is represented in $I_T^* I_R$. The external field can also reinforce or weaken the self-field depending on the relative directions and relative strengths of the fields, which is represented in γ_R and therefore a factor which depends on geometry. γ_T and γ_R can be different because the Tx winding and the Rx winding are not necessarily identical; therefore, the geometric effect of the opposing external magnetic field is not necessarily symmetric. The Tx coil current also contributes to the loss because of the external proximity effect, which is dissipated in the Rx coil;[6] eddy currents are created in the Rx coil from the time-varying magnetic field from the Tx coil current. The eddy current can be modeled as an independent winding [33], [34] that is electromagnetically coupled to the Tx coil. The eddy current loss is then a real power transferred from the Tx coil to the eddy winding and can be represented by the source current (Tx coil current) and the effective resistance $R_{T:r}$. Appendix A introduces the eddy winding model and derives the eddy current losses dissipated in the Rx coil. $R_{T:r}$ is the effective resistance that encapsulates: 1) the magnetic coupling between the Tx coil and an eddy current winding in the Rx coil, and 2) the effect of the impedance in the eddy current winding.

$P_{\text{W, Rx}}$ represents the Rx winding loss, measured at the Rx coil's electrical terminal as a part of the output power, where R_R, γ_T, and $R_{R:t}$ are defined in the same manner as for the Tx winding loss. Note that $\gamma_R R_T$ and $\gamma_T R_R$ are equal because of reciprocity.

Input power P_{Tx} in (13) and output power P_{Rx} in (14) can be formulated from the terminal voltages (89) and (90) of the winding loss model in Appendix A

$$P_{\text{Tx}} = \text{Re}\left\{j\omega M_{R:T} I_R I_T^*\right\} + \text{Re}\left\{I_T^* I_T + \gamma_R I_T^* I_R\right\} R_T + \text{Re}\left\{I_T^* I_T\right\} R_{T:r} \quad (17)$$

[6]The quantification of the loss can be confirmed by examining the difference in input power between the two cases when the Tx coil is driven by current source I_T: 1) When the Rx coil does not exist physically; and 2) when the Rx coil is physically present, but open-circuited ($I_R = 0$).

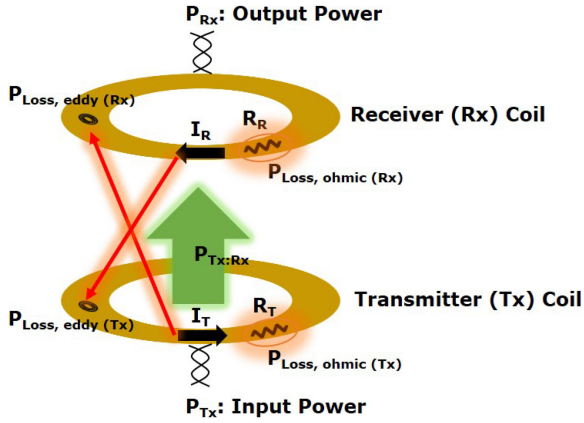

Fig. 7. Power flow in WPT. Input power P_{Tx}, measured at the Tx coil terminal, is composed of: 1) $P_{\text{Tx:Rx}}$ in (12); 2) $P_{\text{Loss, ohmic (Tx)}}$, ohmic losses due to the Tx coil winding resistance R_T; and 3) $P_{\text{Loss, eddy (Rx)}}$, the external proximity effect loss, dissipated in the Rx coil, generated by the Tx coil current I_T. At the Rx coil, $P_{\text{Tx:Rx}}$ is received and losses are incurred, which are composed of: 1) $P_{\text{Loss, ohmic (Rx)}}$, ohmic losses due to the Rx coil winding resistance R_R; and 2) $P_{\text{Loss, eddy (Tx)}}$, the external proximity effect loss, dissipated in the Tx coil, generated by the Rx coil current I_R. The output power P_{Rx} measured at the Rx coil terminal is then the difference between $P_{\text{Tx:Rx}}$ and the incurred loss.

$$P_{\text{Rx}} = \text{Re}\left\{j\omega M_{T:R} I_T I_R^*\right\} + \text{Re}\left\{I_R^* I_R + \gamma_T I_R^* I_T\right\} R_R + \text{Re}\left\{I_R^* I_R\right\} R_{R:t}. \quad (18)$$

Fig. 7 shows the power flow in WPT. Observe that input and output terminal power commingle winding losses and therefore cannot disaggregate losses properly: 1) Input power P_{Tx} aggregates winding losses, which are the ohmic losses dissipated in the Tx coil $P_{\text{Loss,ohmic(Tx)}}$ and the eddy current losses dissipated in the Rx coil $P_{\text{Loss,eddy(Rx)}}$ and 2) output power P_{Rx} also aggregates winding losses, which are the ohmic losses dissipated in the Rx coil $P_{\text{Loss,ohmic(Rx)}}$ and the eddy current losses dissipated in the Tx coil $P_{\text{Loss,eddy(Tx)}}$. For example, when the Rx coil is open-circuited, the output power P_{Rx} is zero, but there is heat dissipation in the Rx coil from the Tx coil current, which should be attributed to the Rx coil. It is worth noting that the transfer-power that is useful for metering comprises the principal transfer-power and the eddy current losses

$$P_{\text{Transfer}} = P_{\text{Tx:Rx}} + P_{\text{Loss,eddy(Rx)}} - P_{\text{Loss,eddy(Tx)}}. \quad (19)$$

For the purpose of fair metering, we can redistribute power losses based on the Tx and Rx coils' dissipation $P_{\text{d,Tx}}$ and $P_{\text{d,Rx}}$

$$P_{\text{d,Tx}} = \text{Re}\left\{I_T^* I_T + \gamma_R I_T^* I_R\right\} R_T + \text{Re}\left\{I_R^* I_R\right\} R_{R:t} \quad (20)$$

$$P_{\text{d,Rx}} = \text{Re}\left\{I_R^* I_R + \gamma_T I_R^* I_T\right\} R_R + \text{Re}\left\{I_T^* I_T\right\} R_{T:r} \quad (21)$$

which are in contrast to (15) and (16). Note that what is dissipated in the coil is a combination of 1) the ohmic loss and 2) the external proximity effect (eddy current losses). Equations (20) and (21) explain the eddy current losses in the Tx and Rx coils. This manifests in the example where despite the Rx coil being open-circuited ($I_R = 0$), $P_{\text{d,Rx}}$ is nonzero, yet with a loss generated by the Tx coil current.

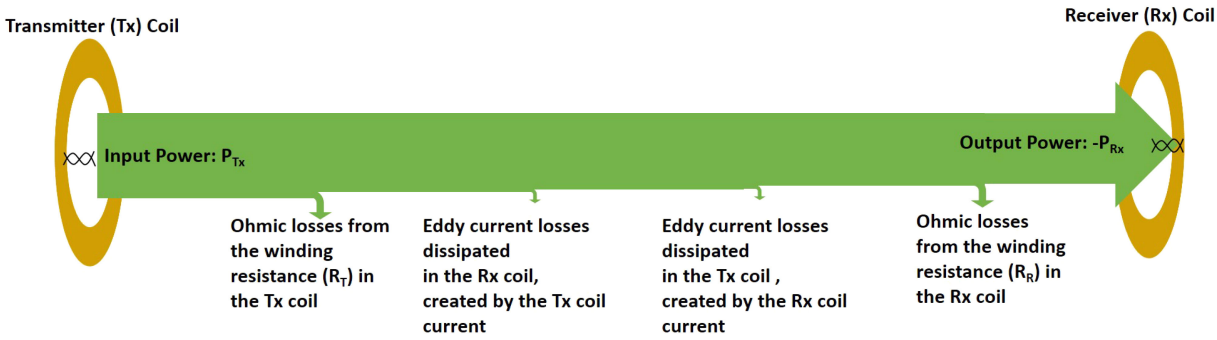

Fig. 8. Power conservation in a WPT system. Transfer-power can be obtained by disaggregating the winding losses from the input and output power.

Power conservation in WPT from the input power to the output power can be shown with an accounting of the winding losses

$$\underbrace{P_{\text{Tx}}}_{\text{Input power at the Tx coil}} = \underbrace{\text{Re}\left\{I_T^* I_T + \gamma_R I_T^* I_R\right\} R_T}_{\text{Ohmic loss from the Tx winding resistance } R_T} + \underbrace{\text{Re}\left\{I_T^* I_T\right\} R_{T:r}}_{\text{Eddy current losses in the Rx coil, generated by } I_{\text{T}}} + \underbrace{\text{Re}\left\{I_R^* I_R\right\} R_{R:t}}_{\text{Eddy current losses in the Tx coil, generated by } I_{\text{R}}} + \underbrace{\text{Re}\left\{I_R^* I_R + \gamma_T I_R^* I_T\right\} R_R}_{\text{Ohmic loss from the Rx winding resistance } R_R} - \underbrace{P_{\text{Rx}}}_{\text{Output power at the Rx coil}}. \quad (22)$$

Note that the negative sign before P_{Rx} accounts for the power consumption in the Rx coil. Fig. 8 illustrates the conservation of power in WPT.

B. Transfer-Power Metering With Losses

In Section II-A, transfer-power is defined from the Poynting vector, which is the electromagnetic power density through space. As shown in Fig. 7, the transfer-power P_{Transfer} for lossy coils is the sum of three power flows: 1) $P_{\text{Tx: Rx}}$: the real power transferred from the Tx to Rx coils, $\text{Re}\{j\omega M_{T:R} I_R I_T^*\}$ in (12), which is the principal transfer-power; 2) $P_{\text{Loss,eddy(Rx)}}$: eddy current loss in the Rx coil; and 3) $P_{\text{Loss,eddy(Tx)}}$: eddy current loss in the Tx coil, so that

$$P_{\text{Transfer}} = \text{Re}\left\{j\omega M_{R:T} I_R I_T^*\right\} + \left\{I_T^* I_T\right\} R_{T:r} - \left\{I_R^* I_R\right\} R_{R:t}. \quad (23)$$

Metering based on transfer-power explicitly attributes a particular coil's losses as the power it is dissipating as heat, which is consistent with the assertion of the Poynting vector definition. Transfer-power is equal to transmitter coil terminal power minus the Tx coil power dissipation

$$P_{\text{Transfer (}Tx\text{-referenced)}} = P_{\text{Tx}} - P_{\text{d,Tx}}. \quad (24)$$

In other words, transmitters Tx (providers) automatically pay for the cost of $P_{\text{d,Tx}}$ if metering is based on transfer-power. Similarly, receivers Rx (customers) automatically pay for their own power dissipation $P_{\text{d,Rx}}$ along with the power they receive for consumption. From the receiver side, the transfer-power can be represented by

$$P_{\text{Transfer (}Rx\text{-referenced)}} = -P_{\text{Rx}} + P_{\text{d,Rx}}. \quad (25)$$

For example, a customer can reduce their dissipation (from ohmic and transmitter-induced eddy current loss), hence their cost of energy, by using a higher quality litz wire.

C. Extraction of Winding Loss Model From FEM Simulations

We can calculate winding losses from FEM simulations; we can show how the power and loss distribute among the various mechanisms for various Tx and Rx coil configurations to study how, in practice, power partitions in WPT charging. Circular versions of wireless charging coils based on SAE J2954 [35] were evaluated using finite element analysis using COMSOL. Different transmitter and receiver coil radii (r_T and r_R), air gaps ($d_{T:R}$), windings (N_T and N_R), and power classes, representing a wide range of standardized options, were selected. Appendix B presents the details of the simulations and calculations, and the coil specifications for Table VI.

Two-dimensional axisymmetric simulations were performed with the Tx and Rx coils driven by current sources. Although in practice, litz wire is typical, solid wire was used in these analyses as worst-case examples. The Tx coil currents were chosen to be the maximum current for each power class, and the Rx coil currents were selected to satisfy the maximum power level for the class, both specified in [35].

Table I presents the principal transfer-power $P_{\text{Tx:Rx}}$, ohmic losses ($P_{\text{ohmic,Tx}}$ and $P_{\text{ohmic, Rx}}$), and eddy current losses ($P_{\text{eddy, Tx}}$ and $P_{\text{eddy, Rx}}$) as a percentage of the input power for each coil specification. As expected (24) and (25) give identical results for each coil configuration. The results are compared graphically in Fig. 9. The power flow from the Tx to Rx coil $P_{\text{Tx:Rx}}$ is the dominating quantity, while ohmic losses are the greatest portion of the winding losses. The worst case for the percentage eddy current loss was 1.12 %, dissipated in the Rx coil for the WPT2/Z1 class.

IV. Faraday Coil Transfer-Power Measurement

FC-TPM is a non-contact electromagnetic method to measure *transfer-power* through an intervening space by making

TABLE I
LOSS BUDGET FOR VARIOUS WPT COIL CONFIGURATIONS (SOLID WIRE; SPIRAL WINDING): POWER BUDGET

Power Class	Z-Class	P_{Tx}(kW)	$P_{\text{Tx:Rx}}$(%)	$P_{\text{ohmic,Tx}}$ (%)	$P_{\text{ohmic,Rx}}$(%)	$P_{\text{eddy,Tx}}$(%)	$P_{\text{eddy,Rx}}$(%)	P_{Rx}(kW)	η (%)
WPT1	Z1	3.91	91.2	8.30	1.67	1.94E-03	0.505	3.50	89.5
	Z2	4.11	91.3	7.89	2.20	1.62E-03	0.822	3.66	89.1
	Z3	4.08	91.7	7.96	0.737	3.14E-03	0.339	3.71	91.0
WPT2	Z1	8.83	87.8	11.3	0.454	1.23E-03	0.995	7.71	87.3
	Z2	8.44	87.7	11.8	0.241	1.29E-03	0.538	7.38	87.5
	Z3	8.83	88.5	11.3	0.215	1.45E-03	0.242	7.79	88.3
WPT3	Z1	12.9	91.8	7.70	0.483	2.07E-03	0.513	11.8	91.3
	Z2	12.3	91.5	8.08	0.383	2.05E-03	0.369	11.2	91.2
	Z3	12.6	91.9	7.89	0.331	2.23E-03	0.169	11.5	91.6

$P_{\text{Tx:Rx}}$, $P_{\text{ohmic,Tx}}$, $P_{\text{ohmic,Rx}}$, $P_{\text{eddy,Tx}}$, $P_{\text{eddy,Rx}}$ are percentages of the input power P_{Tx}.
η is the Tx-to-Rx coil efficiency in percent, $P_{\text{Rx}}/P_{\text{Tx}} \times 100$.

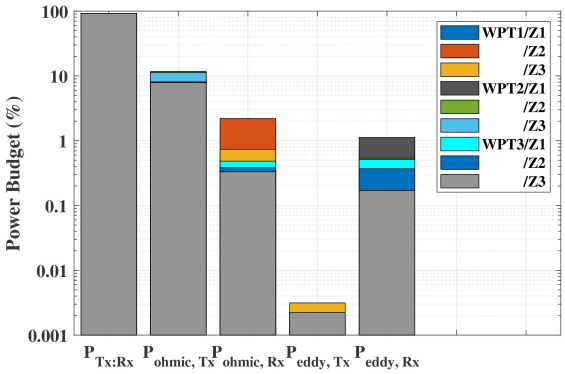

Fig. 9. Budget for the transfer-power and loss as a percentage of the input Tx power P_{Tx} for various coil configurations and power levels.

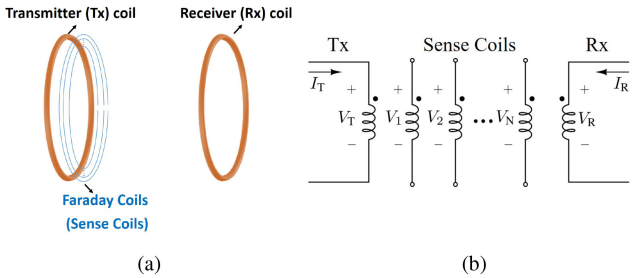

Fig. 10. Non-contact and open-circuited Faraday sense coils are employed in the WPT system to measure the transfer-power. (a) Conceptual diagram. (b) Transformer equivalent circuit diagram.

inferences based on sampling the electromagnetic fields using open-circuited Faraday sense coils. FC-TPM employs the voltages from open-circuited sense coils, as shown in Fig. 10, which are electromagnetically coupled to the Tx and Rx coils to reconstruct the transfer-power.

FC-TPM is the first among methods in EV charging to measure the power flow through space, resulting in fair metering. Advantages of FC-TPM include the following.

1) Accuracy that is independent of self-inductance and ohmic loss of Tx and Rx coils, power electronics (e.g., compensation circuit topologies), and electrical loads of the Rx side.
2) Accuracy that is insensitive to coil misalignment, operating frequencies, and various coil wire types (e.g., solid and litz wires).

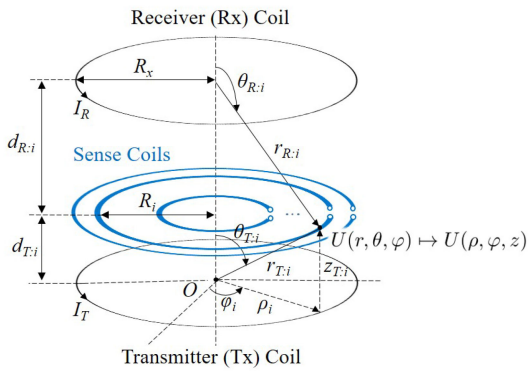

Fig. 11. Non-contact open-circuited sense coils are placed between the Tx and Rx current loops. The sense coil voltages are induced by the magnetic fields from the Tx and Rx currents. The Poynting vectors can be mapped to the sense coil voltages.

3) Small footprint with sense coils that are few in number and diminutive in size whose electromagnetic and physical disturbance is negligible.

This section shows how the sense coil voltages reconstruct the real power flow in WPT. First, we derive the Poynting vectors from the sense coil voltages to prove that FC-TPM directly measures the electromagnetic power flow through the air gap. Then, we derive the transfer-power from the sense coil voltages using the transformer-model, which reveals the benefit of using geometric parameters and leads to calibration strategies for FC-TPM.

A. Mapping the Sense Coil Voltages to the Poynting Vector

The Poynting vector can be represented by sense coil voltages from which transfer-power can ultimately be derived. Sense coils sample the electromagnetic field from which the Poynting vector can be reconstructed. If the sense coils are placed coaxially with the Tx and Rx coils, as shown in Fig. 11, a sense coil voltage V_i is induced by the $\hat{z}$ component of the magnetic field from (4)

$$V_i = -\oint \vec{E}_i \cdot d\vec{l} \tag{26}$$

$$= \frac{d}{dt} \iint_{\mathcal{S}} B_z \hat{z} \cdot d\vec{s} \tag{27}$$

$$= g\left(d_{T:i}, R_i\right)\ j\omega I_T + g\left(d_{R:i}, R_i\right)\ j\omega I_R \tag{28}$$

where

$$g\left(d_{X:i}, R_i\right) = \frac{\mu_0 A R_i^2}{2\left({d_{X:i}}^2 + R_i^2\right)^{\frac{3}{2}}}. \tag{29}$$

Note that $d_{X:i}$ is the distance between coil X and sense coil i; R_i is the radius of sense coil i; $A = \pi R_x^2$ is the Tx and Rx loop area, where R_x is assumed to be much smaller than the distance between the two coils $d_{T:R}$ ($R_x \ll d_{T:R}$) from the magnetic dipole approximation of the Tx and Rx loops. What results from (28) and (29) is that the Tx and Rx coil currents (I_T and I_R) can be reconstructed by a linear combination of the pair of sense coil voltages (V_i and V_j)

$$I_T = \frac{g\left(d_{R:j}, R_j\right)}{\lambda}\ \frac{V_i}{j\omega} + \frac{-g\left(d_{R:i}, R_i\right)}{\lambda}\ \frac{V_j}{j\omega} \tag{30}$$

$$I_R = \frac{-g\left(d_{T:j}, R_j\right)}{\lambda}\ \frac{V_i}{j\omega} + \frac{g\left(d_{T:i}, R_i\right)}{\lambda}\ \frac{V_j}{j\omega} \tag{31}$$

where

$$\lambda = g\left(d_{T:i}, R_i\right) g\left(d_{R:j}, R_j\right) - g\left(d_{R:i}, R_i\right) g\left(d_{T:j}, R_j\right). \tag{32}$$

As shown in (5), the Poynting vector can be represented by the Tx and Rx coil currents. In other words, determining the Tx and Rx coil currents from the sense coil voltages in (30) and (31) enables one to find the Poynting vector.

The real part of the time-averaged complex Poynting vector is

$$\mathrm{Re}\left\{\vec{S}\right\} = \mathrm{Re}\left\{S_z\right\} \tag{33}$$

$$= \mathrm{Re}\left\{E_\varphi \times H_\rho^*\right\} \tag{34}$$

$$= \frac{m(r,\theta)}{\lambda}\frac{1}{\omega}\mathrm{Im}\left\{V_i V_j^*\right\} \tag{35}$$

where

$$m(r,\theta) = \frac{3\mu_0 A^2}{16\pi^2 r^5}\sin 2\theta \sin\theta. \tag{36}$$

λ is the geometric parameter, determined by the sense coil positions. In summary, the Poynting vector at any point in the plane of interest can be mapped by the imaginary part of the complex conjugate pair of sense coil voltages $\mathrm{Im}\{V_i V_j^*\}$.

B. Theory of FC-TPM Using the Transformer Model

The sense coil voltages can represent transfer-power through the transformer model. In this and the following two sections (IV-C and IV-D), we neglect external eddy current losses.[7] Because there are no eddy current windings, the open-circuited sense coil voltages are induced only by the Tx and Rx coil currents.

[7]This assumption elucidates the principle of accurate FC-TPM over the Rx coil's misalignment and corresponding calibration strategy in Section IV-C. The eddy current loss and hence the winding can be taken into account by increasing the matrix's dimension in (38) with four sense coils to include eddy currents I_t, I_r and corresponding mutual inductances, as shown in (63) in Section IV-E.

The sense coil voltages V_i in the frequency domain are

$$V_i = j\omega M_{T:i} I_T + j\omega M_{R:i} I_R\,. \tag{37}$$

The Tx and Rx coil currents (I_T and I_R) can be derived from two sense coil voltages (V_i and V_j)

$$\begin{pmatrix} I_T \\ I_R \end{pmatrix} = \frac{1}{\mathcal{D}}\begin{pmatrix} M_{R:j} & -M_{R:i} \\ -M_{T:j} & M_{T:i} \end{pmatrix}\begin{pmatrix} \frac{V_i}{j\omega} \\ \frac{V_j}{j\omega} \end{pmatrix} \tag{38}$$

$$\mathcal{D} = M_{T:i}M_{R:j} - M_{R:i}M_{T:j} \tag{39}$$

where $M_{T:i}$ and $M_{R:i}$ are the mutual inductances from the Tx and Rx coils to the i^{th} sense coil.

The transfer-power in (12) is represented in terms of the mutual reactance $\omega M_{R:T}$ between the Tx and Rx coils, and the Tx and Rx coil currents (I_T and I_R). Sense coil voltages (V_i and V_j) can, thus, represent the transfer-power

$$P_{\text{Transfer}}(\omega) = \mathrm{Re}\left\{j\omega M_{R:T} I_R(\omega) I_T(\omega)^*\right\} \tag{40}$$

$$= \frac{1}{\kappa_{ij}}\mathrm{Im}\left\{V_i(\omega) V_j^*(\omega)\right\} \tag{41}$$

where

$$\kappa_{ij} = \omega\sqrt{L_i L_j}\frac{k_{T:i}k_{R:j} - k_{T:j}k_{R:i}}{k_{R:T}}. \tag{42}$$

We denote $k_{m:n}$ as the coupling coefficient between any two coils m and n, where $k_{m:n} = M_{m:n}/\sqrt{L_m L_n}$. κ_{ij} is a function of the coupling coefficients between coils and the self-inductances of the sense coils (L_i and L_j) at angular frequency ω. In the frequency domain, the calculated component of transfer-power at each frequency point can be converted to the average power in watts (p_{Transfer}) through Parseval's theorem [36]

$$p_{\text{Transfer}} = \frac{1}{N}\sum_{\omega=0}^{N-1} P_{\text{Transfer}}(\omega) \tag{43}$$

where N is the number of data samples and P_{Transfer} is calculated from the discrete-time Fourier transform (DTFT) of the voltage and current signals. Total power in the time-domain is equal to that in the frequency domain.

C. Accurate FC-TPM Throughout Rx Coil Misalignment

Misalignment between the Tx (energy charging stations) and Rx coils (EVs) is unavoidable; even an autonomous system can have misalignment. In fact, SAE J2954 [35] certifies misalignment up to 10 cm for a 45 cm diameter coil. FC-TPM must therefore be accurate over that misalignment range, as illustrated in Fig. 12.

FC-TPM as metering is practical for energy service stations in that only sense coil voltages are needed for measurement during charging. In the previous Section (IV-B), the corresponding geometric parameters were required to be constant so that they could be calibrated in advance. As detailed in (41) and (42), the geometric parameter κ_{ij} is needed together with the sense coil voltages to determine transfer-power.

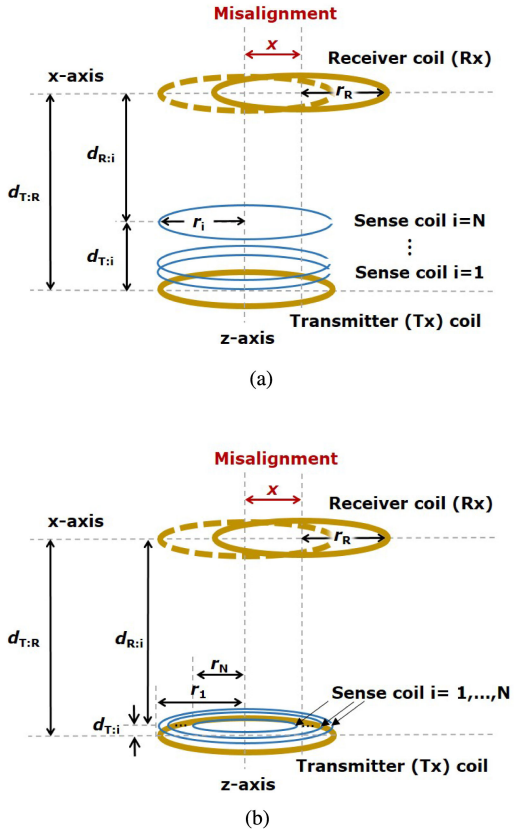

Fig. 12. Configurations of the Tx, Rx, and sense coils with Rx coil misalignment. (a) The sense coils are placed coaxially with the Tx coil, which can be vertically stacked. (b) Coplanar sense coils are on the same plane to have a low profile above the Tx coil. The radii of the sense coils are differentiated so that independent information regarding misalignment can be implicitly obtained.

However, coil misalignment makes κ_{ij} vary. This is so because κ_{ij} is a function of coupling coefficients ($k_{R:j}$, $k_{R:i}$, and $k_{R:T}$) that vary over misalignment.[8] To resolve the problem of parameter variation, we employ multiple sense coils to collect more information, where nonvarying geometric parameters can be obtained over misalignment to determine the transfer-power. We found that a linear combination of pairwise-products of sense coil voltages determine the transfer-power accurately. The coefficients for the linear combination are geometric parameters that do not vary over misalignment. In fact, neither knowledge nor an explicit measurement of misalignment is needed to determine the transfer-power.

Despite the significant misalignment allowed for SAE J2954, the coupling coefficients from the Tx and sense coils to the Rx coil are well-approximated by quadratic functions (i.e., second-order polynomials) over the Rx coil misalignment. This quadratic approximation explains how a linear combination of pairwise-product of sense coil voltages can accurately determine transfer-power at any misalignment, with constant coefficients for the linear combination, hence allowing calibration. In fact, calibration requires neither knowledge nor explicit measurement of misalignment.

[8]A practical design requires Tx and sense coils to be stationary making $k_{T:i}, k_{T:j}$ constant over Rx coil misalignment.

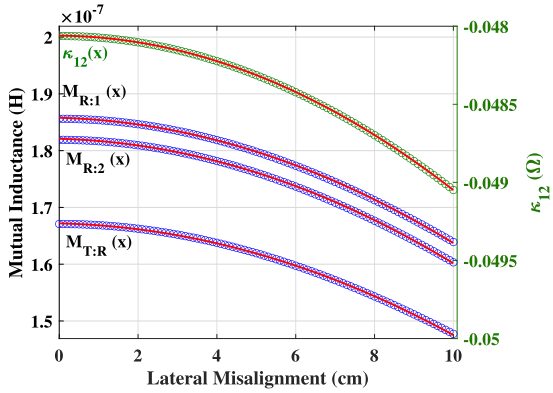

Fig. 13. Numerical results of the relevant mutual inductances (blue-dots): 1) Tx-to-Rx; and 2) Rx-to-sense-coils. The geometric parameter $\kappa_{12}(x)$ (green-dots) in (45) for two coplanar sense coils (sense coil 1 and 2, specified in Table II) are plotted over Rx coil misalignment. Red lines are the corresponding second-order polynomial fits.

In this section, we show how the coupling coefficients can be approximated by quadratic functions of misalignment. We then present a formulation to determine transfer-power that is accurate over misalignment using multiple sense coil voltages.

1) Quadratic Approximation of Coupling Coefficient Variation Over Misalignment: When the coupling coefficient from the Tx to Rx coil varies quadratically over the Rx coil's misalignment, it is advantageous to choose sense coil positions and radii so that the coupling coefficients from the sense coils to the Rx coil are also quadratic dominant. It is important to note that the coupling coefficient functions are positive definite; the quotient of positive definite quadratic functions is also quadratic dominant, albeit over a narrower interval. Sense coils that are coaxially positioned with the Tx coil are especially good candidates for quadratic dominant coupling coefficients. In the following Section IV-C2, we show how least-squares optimization of a parameterization of coupling coefficients based on quotients that form a quadratic dominant function is particularly good at determining transfer-power.

We derive a quadratic approximation for the mutual inductance and hence the coupling coefficient from Grover [37] for two circular filaments with lateral misalignment. The quadratic approximation is a Taylor expansion with respect to lateral misalignment. In bounding the Lagrange remainder, we show that this second-order Taylor approximation is accurate over the misalignment range of interest, which we detail in Appendix C. In Fig. 13, we show the calculated results for the 1) the mutual inductance, and hence the coupling coefficient, and 2) the geometric parameter κ_{ij} for the Tx and Rx coils using the numerical model for circular filaments in [38].

The mutual inductances and κ_{ij} are very nearly quadratic with a *coefficient of determination* $R^2 > 0.999$.[9] We further investigated the quadratic dependence for different sense coil positions and radii using R^2. Fig. 14 shows that sense coil positions closer to the Tx coil are better.

2) FC-TPM Formulation Over Rx Coil Misalignment: Sense coil voltages implicitly contain information about the Rx coil

[9]R-squared (R^2) indicates the goodness of fit, ranging from 0 to 1. $R^2 = 1$ means that there is no error in the fitting [39].

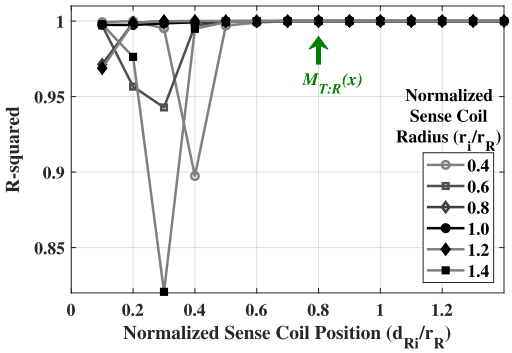

Fig. 14. Numerical results of R-squared values of the second order of polynomial fit of mutual inductance from the Rx coil over misalignment were plotted for different geometries. The R-squared values were obtained by the curve fitting toolbox (MATLAB R2018b).

misalignment. When combined with functions that implicitly contain information about the sense coil positions and sizes, transfer-power can be determined with minimal error from misalignment.

The transfer-power represented by (41) and (42) is a function of the lateral misalignment x of the Rx coil

$$P_{\text{Transfer}}(x) = \frac{1}{\kappa_{ij}(x)} \Big\langle V_i(x), V_j(x) \Big\rangle \tag{44}$$

where

$$\kappa_{ij}(x) = \omega \sqrt{L_i L_j} \frac{k_{T:i} k_{R:j}(x) - k_{T:j} k_{R:i}(x)}{k_{R:T}(x)} \tag{45}$$

$$\langle V_i, V_j \rangle \triangleq \operatorname{Im} \left\{ V_i V_j^* \right\}. \tag{46}$$

Note that $V_{i,j}(x)$ are sense coil voltages at a particular Rx coil misalignment x. We define $\langle V_i, V_j \rangle$ as the pairwise-product of sense coil voltages, where V_i and V_j are complex scalars. For power metering, the Tx and sense coils have fixed positions, whereas the EVs (Rx coils) drive in to charge; therefore, the coupling coefficients between Tx and sense coils ($k_{T:i}$ and $k_{T:j}$) do not change.

If we use (44) to determine transfer power, the misalignment x and every coupling coefficient as a function of x must be explicitly and accurately known. However, in using multiple sense coils, we can transform the overdetermined set of sense coil voltages to a function that determines transfer-power from these sense coil voltages alone. We will show that this function can be simply calibrated over the span of misalignment, but without needing a measurement of misalignment at all.

In using multiple sense coils, the pairwise-product of voltages from each unique pair $\langle V_i, V_j \rangle$ can be linearly combined and scaled by corresponding coefficients α_{ij}

$$\sum_{i,j \in Q} \alpha_{ij} \Big\langle V_i(x), V_j(x) \Big\rangle = P_{\text{Transfer}}(x) \left\{ \sum_{i,j \in Q} \alpha_{ij} \kappa_{ij}(x) \right\}$$
$$Q = \Big\{ (i,j) \in \mathbb{N}^2 \,\Big|\, i \le N, j \le N, \text{ and } i < j \Big\} \tag{47}$$

where N is the number of sense coils.

As discussed earlier, the function $\kappa_{ij}(x)$ is well approximated by a quadratic polynomial

$$\kappa_{ij}(x) \approx p_{ij} + q_{ij} x + r_{ij} x^2$$
$$\text{where } p, q, r \in \mathbb{R}. \tag{48}$$

If we choose α_{ij} so that

$$\sum_{i,j \in Q} \alpha_{ij} \kappa_{ij} \approx \sum_{i,j \in Q} \alpha_{ij} p_{ij} + \sum_{i,j \in Q} \alpha_{ij} q_{ij} x + \sum_{i,j \in Q} \alpha_{ij} r_{ij} x^2 \tag{49}$$
$$\approx 1,$$

where

$$\sum_{i,j \in Q} \alpha_{ij} p_{ij} \approx 1, \sum_{i,j \in Q} \alpha_{ij} q_{ij} \approx 0, \sum_{i,j \in Q} \alpha_{ij} r_{ij} \approx 0$$
$$\alpha_{ij} \in \mathbb{R} \tag{50}$$

and perform a least-squares optimization to obtain α_{ij}

$$\underset{\alpha_{ij}}{\text{minimize}} \quad \left\| P_{\text{Transfer}}(x) - \sum_{i,j \in Q} \alpha_{ij} \Big\langle V_i(x), V_j(x) \Big\rangle \right\|_2$$
$$\text{subject to } \alpha_{ij} \in \mathbb{R} \tag{51}$$

then the transfer-power can be determined despite misalignment from the linear combination of unique pairwise-products of sense coil voltages

$$P_{\text{Transfer}} = \sum_{i,j \in Q} \alpha_{ij} \Big\langle V_i, V_j \Big\rangle$$
$$Q = \Big\{ (i,j) \in \mathbb{N}^2 \,\Big|\, i \le N, j \le N, \text{ and } i < j \Big\} \tag{52}$$

where $V_i = V_i(x)$ and $V_j = V_j(x)$ are only voltage measurements and implicit functions of x; N is the number of sense coils. Note that the geometric parameters α_{ij}, which are calibrated initially, are constant (independent of x).

D. Calibration of Constant Geometric Parameters Over Misalignment and FC-TPM Numerical Results

In this section, we explain how the geometric constants in Section IV-C2 can be calibrated. We then numerically evaluate FC-TPM over misalignment using well-known models from the literature.

1) Formulating the Calibration Matrix and Vector: The calibration of the geometric parameters α_{ij} requires sense coil voltage measurements and transfer-power data from a reference standard. The sense coil voltage measurements are combined as

uniquely paired products in a data matrix

$$\mathbf{W} = \begin{pmatrix} \langle V_1(x_1,Z_1),V_2(x_1,Z_1)\rangle & \dots & \langle V_i(x_1,Z_1),V_j(x_1,Z_1)\rangle \\ \vdots & \ddots & \vdots \\ \langle V_1(x_m,Z_1),V_2(x_m,Z_1)\rangle & \dots & \langle V_i(x_m,Z_1),V_j(x_m,Z_1)\rangle \\ \langle V_1(x_1,Z_2),V_2(x_1,Z_2)\rangle & \dots & \langle V_i(x_1,Z_2),V_j(x_1,Z_2)\rangle \\ \vdots & \ddots & \vdots \\ \langle V_1(x_m,Z_2),V_2(x_m,Z_2)\rangle & \dots & \langle V_i(x_m,Z_2),V_j(x_m,Z_2)\rangle \\ \vdots & \ddots & \vdots \\ \vdots & \ddots & \vdots \\ \langle V_1(x_m,Z_n),V_2(x_m,Z_n)\rangle & \dots & \langle V_i(x_m,Z_n),V_j(x_m,Z_n)\rangle \end{pmatrix}. \tag{53}$$

The transfer-power corresponding to each row of $\mathbf{W}$ is contained in the elements of column vector $\mathbf{p}$

$$\mathbf{p} = [P_{\text{Transfer}}(x_1, Z_1)\ P_{\text{Transfer}}(x_2, Z_1) \cdots P_{\text{Transfer}}(x_m, Z_n)]^{\intercal}. \tag{54}$$

Each row of $\mathbf{W}$ corresponds to a particular measurement condition (e.g., misalignment, power, load, etc.). The number of unique pairings for the the pairwise-product of sense coil voltages from N sense coils is $N_w = {}^{N}\mathrm{C}_2$. For l data points of variation that consists of m data points of misalignment ($x_{1,\dots,m}$) and n data points of Rx coil loading ($Z_{1,..,n}$): $l = mn$, $\mathbf{W} \in \mathbb{R}^{l\times N_w}$, and $\mathbf{p} \in \mathbb{R}^{l\times 1}$.

The data for calibration needs to span the space of variation, which includes geometric variation (e.g., misalignment) and load. The variation in load needs to span the real impedances corresponding to the required measurement range for transfer-power.

It is worth noting that the variation encapsulated in $\mathbf{W}$ and $\mathbf{p}$ does not have to be uniform, nor does the explicit domain of variation (e.g., actual misalignment displacement x) need to be measured.

The vector of geometric parameters $\alpha_{ij} \in \mathbb{R}^{N_w\times 1}$ for N sense coils is

$$\boldsymbol{\alpha} = \begin{bmatrix} \alpha_{12} & \alpha_{13} & \dots & \alpha_{ij} \end{bmatrix}^{\intercal}. \tag{55}$$

From (52)

$$\mathbf{W}\,\boldsymbol{\alpha} = \mathbf{p} \tag{56}$$

which is overdetermined, allowing the calculation, and hence calibration of $\boldsymbol{\alpha}$ using the least-squares method

$$\boldsymbol{\alpha} = (\mathbf{W}^{\intercal}\mathbf{W})^{-1}\,\mathbf{W}^{\intercal}\mathbf{p}\,. \tag{57}$$

2) Coil Configurations: Two different placements of sense coils were considered for the numerical analysis, as shown in Fig. 12(a) and (b).

(a) *Vertically stacked sense coils*: The N sense coils are vertically stacked above the Tx coil at 1 cm intervals. The radii of the Tx, Rx, and sense coils are identically 25 cm.

(b) *Coplanar sense coils (low-profile)*: All N sense coils are concentric and placed on the same plane, which is 1 cm above the Tx coil. The sense coil radii varied from 26 to 23.5 cm, decreasing at 0.5 cm intervals.

TABLE II
CONFIGURATIONS OF THE TX, RX, AND SENSE COILS

Parameters	Value	Parameters	Value
r_T,r_R	25 cm	$d_{T:R}$	20 cm
r_i (Stacked)	25 cm	$d_{T:i}$ (Stacked)	$i\cdot 1$ cm
r_i (Coplanar)	26 cm - $(i-1)\cdot 0.5$ cm	$d_{T:i}$ (Coplanar)	1 cm

For each case, the Tx, Rx, and sense coils have the same center axis (coaxial). Table II presents the specifications for each coil configuration.

3) Numerical Results: Mutual inductances were obtained from a well-known circular filament model [38] over the Rx coil misalignment x. The model assumptions include: i) Concentrated windings as shown in Fig. 12; ii) fundamental frequency only; and iii) no measurement noise. The Tx and Rx coils are driven by current sources. The transfer-power and sense coil voltages were calculated with (12) and (37), respectively, at each misalignment. The equivalent circuit for the numerical model is shown in Fig. 10(b). The geometric parameters α_{ij} were calibrated using sense coil voltages and transfer-power; the accuracy of FC-TPM was then evaluated using leave-one-out cross-validation (LOOCV) [40].[10] FC-TPM accuracy was evaluated for different numbers of sense coils (from two to six). For these numerical results, $m = 11$ misalignment data points (0–10 cm at 1-cm intervals) and $n = 6$ load data points were used to calibrate α_{ij}.

The FC-TPM errors over misalignment were calculated for each data point using LOOCV. The percentage errors are calculated between the standardized value $P_{\text{Transfer}}(x_m, Z_n)$, and the reconstructed value $\hat{P}_{\text{Transfer}}(x_m, Z_n)$

$$\varepsilon(x_m, Z_n) = \frac{\hat{P}_{\text{Transfer}}(x_m, Z_n) - P_{\text{Transfer}}(x_m, Z_n)}{P_{\text{Transfer}}(x_m, Z_n)} \times 100\ (\%) \tag{58}$$

where

$$P_{\text{Transfer}}(x_m, Z_n):\ \text{Reference standard transfer-power}$$
$$= \mathrm{Re}\left\{ j\omega M_{R:T}(x_m) I_R(Z_n) I_T(Z_n)^* \right\} \tag{59}$$

$\hat{P}_{\text{Transfer}}\ (x_m, Z_n)$: Transfer-power reconstructed with FC-TPM

$$= \sum_{i,j\in Q} \alpha_{ij} \Big\langle V_i(x_m, Z_n), V_j(x_m, Z_n) \Big\rangle. \tag{60}$$

Fig. 15(a) and (b) show the FC-TPM errors over misalignment for two different sense coil placements, as defined in Fig. 12. We plotted the worst-case absolute error percentages of FC-TPM

$$\Big|\varepsilon(\mathbf{u})\Big|_{\max} \triangleq \max_k |\varepsilon(\mathbf{u}_k)| \tag{61}$$

where $\mathbf{u}_k$ is the vector of parameter variations over which the error is calculated. The worst-case absolute errors at each lateral

[10] In cross-validation, the data are split into two disjoint subsets: A calibration set and a validation set. The calibration is performed with the calibration set, which excludes the validation set. The accuracy of FC-TPM was evaluated with the validation set using the calibrated parameters. In LOOCV, the validation consists of one data point, and the calibration set consists of the other $l-1$ data points.

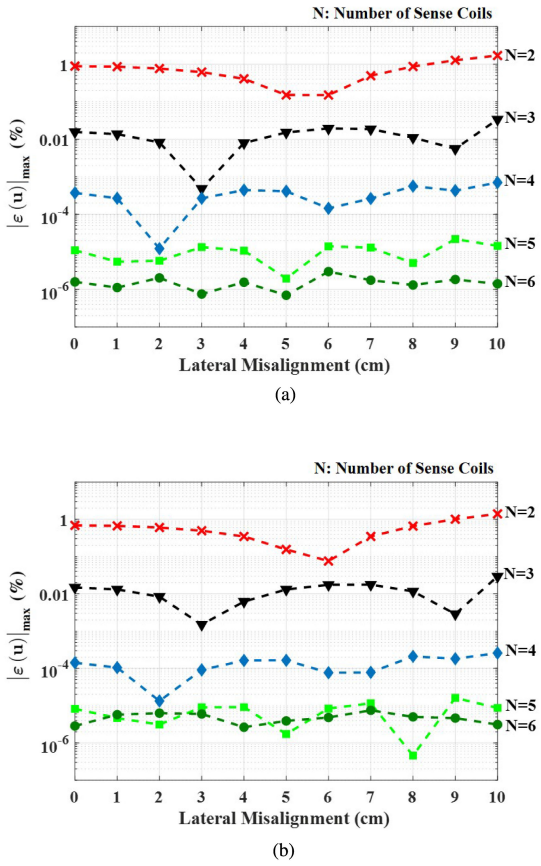

Fig. 15. Results from the numerical model, verifying the accuracy of FC-TPM over misalignment. (a) Sense coils were vertically stacked coaxially at 1-cm intervals above the Tx coil, as shown in Fig. 12(a). (b) Coplanar sense coils were placed coaxially, 1 cm above the Tx coil, as shown in Fig. 12(b). The radii of the sense coils decrease from 26 at 0.5-cm intervals.

misalignment x were calculated and plotted in Fig. 15, where $\mathbf{u}_k = [x \quad Z_k]$.

For both sense coil configurations, the errors were nearly constant over the misalignment with an increasing number of sense coils resulting in lower error. The lowest percentage errors were approximately $10^{-6}\%$ for six sense coils (green circles). Coplanar sense coils have a lower profile and hence are more practical for deployment in charging stations; these results show that coplanar sense coils have comparable performance to coaxial sense coils that are not coplanar. Sensor placement and sizing are analyzed over tradeoffs in Section V-B to corroborate the performance of coplanar configurations relative to other configurations.

Similarly, FC-TPM can be accurate over changes in the distance $d_{T:R}$ between the Tx and Rx coils. FC-TPM over the variations $\Delta d_{T:R}$ of the distance $d_{T:R}$ was numerically evaluated; $\Delta d_{T:R}$ ranged from -5 to 5 cm, resulting in the change in distance between the Tx and Rx coils from 15 to 25 cm, where the nominal distance $d_{T:R}$ was 20 cm. Coplanar sense coils were employed in Table II. FC-TPM accuracy was evaluated for 66 data points, which consisted of 11 data points of distance variations $\Delta d_{T:R}$ (-5 to 5 cm at 1-cm intervals) and 6 load data points. We plotted the worst-case absolute error percentage of FC-TPM at each $\Delta d_{T:R}$ in Fig. 16; the errors

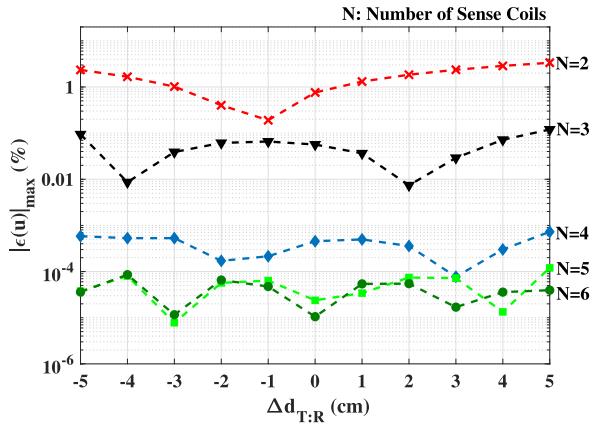

Fig. 16. Results from the numerical model, verifying the accuracy of FC-TPM over $\Delta d_{T:R}$. The nominal distance between Tx and Rx coils $d_{T:R} = 20$ cm when $\Delta d_{T:R} = 0$.

are nearly consistent over $\Delta d_{T:R}$ with an increasing number of sense coils resulting in a lower error. The lowest percentage errors are below $10^{-4}\%$ for six sense coils (green-circles).

E. FC-TPM With Eddy Currents, Rx Coil Misalignment, Different Litz-Wire Types, and Different Operating Frequencies

Eddy currents in the Tx and Rx coils not only add to losses, as presented in Section III but also change the magnetic field geometry by changing the current distribution in the coils nonuniformly. The eddy currents can create a magnetic field with nonnegligible coupling to the opposing coil. In other words, eddy currents induced on the Tx coil create fields that couple to the Rx coil and vice versa.

The induced eddy currents can be represented by additional windings in the transformer and the magnetic field geometry and hence coupling to different coils by the corresponding coupling coefficients. The variation in magnetic field geometry can be caused by a combination of 1) coil misalignment; 2) different wire types (e.g., litz-wire types); and 3) a range of operating frequencies.

In this section, we extend the formulation in Section IV-B and IV-C to include eddy currents and to show how a greater number of sense coils can maintain the accuracy of FC-TPM when there are variations in Rx coil misalignment. Through electromagnetic finite element simulation, we also show that a greater number of sense coils maintain FC-TPM accuracy despite the effects of different types of wire and operating frequencies.

1) FC-TPM With Eddy Currents and Misalignment: When there are eddy currents in the Tx and Rx coils, the sense coil voltages V_i in (37) become

$$V_i = j\omega M_{T:i} I_T + j\omega M_{R:i} I_R + j\omega M_{t:i} I_t + j\omega M_{r:i} I_r. \tag{62}$$

Note that I_t, I_r are the eddy winding currents in the Tx and Rx coils, as discussed earlier in Section III. $M_{t:i}, M_{r:i}$ are the mutual inductances from the eddy windings to the ith sense coil.

For example, Tx, Rx, and eddy winding currents can be derived from four sense coil voltages $V_{1,..,4}$

$$\begin{pmatrix} I_T \\ I_R \\ I_t \\ I_r \end{pmatrix} = \frac{1}{j\omega} \begin{pmatrix} M_{T:1} & M_{R:1} & M_{t:1} & M_{r:1} \\ M_{T:2} & M_{R:2} & M_{t:2} & M_{r:2} \\ M_{T:3} & M_{R:3} & M_{t:3} & M_{r:3} \\ M_{T:4} & M_{R:4} & M_{t:4} & M_{r:4} \end{pmatrix}^{-1} \begin{pmatrix} V_1 \\ V_2 \\ V_3 \\ V_4 \end{pmatrix}. \tag{63}$$

The transfer-power in (23) can be rewritten through (84) in Appendix A

$$\begin{aligned} P_{\text{Transfer}} &= \text{Re}\left\{j\omega M_{R:T} I_R I_T^*\right\} \\ &\quad + \text{Re}\left\{j\omega M_{T:r} I_r I_T^*\right\} - \text{Re}\left\{j\omega M_{R:t} I_t I_R^*\right\} \end{aligned} \tag{64}$$

where $M_{T:r}$ is the mutual inductance between the Tx coil and the Rx coil's eddy current winding; $M_{R:t}$ is the mutual inductance between the Rx coil and the Tx coil's eddy current winding. By combining (63) and (64), the transfer-power can still be determined from a linear combination of the pairwise-product of sense coil voltages

$$P_{\text{Transfer}} = \sum_{i,j \in Q} \lambda_{ij} \left\langle V_i, V_j \right\rangle \tag{65}$$

where

$$\begin{aligned} &Q = \left\{ (i,j) \in \mathbb{N}^2 \,\middle|\, i \le N, j \le N, \text{ and } i < j \right\}, \\ &\left\langle V_i, V_j \right\rangle \triangleq \text{Im}\left\{ V_i V_j^* \right\}. \end{aligned} \tag{66}$$

Detailed expressions for λ_{ij} using an inverse matrix of the mutual inductances in (63) is presented in Appendix D. Note that a minimum of four sense coils $N = 4$ are needed to determine four coil currents (I_T, I_R, I_t, I_r) and hence the transfer-power. If there are more than four sense coils, we can make use of the additional information by choosing four sense coil voltages at a time from the total of N sense coils, from which a total of ${}^N\text{C}_4$ different formulations of (65) are constructed to determine the transfer-power. Each formulation is a linear combination of the pairwise-products of two sense coil voltages chosen out of the four sense coils in the formulation. Using (65), all the formulations can be used to determine the transfer-power, which is detailed in Appendix D.

One can observe in Fig. 17 the effect of differing numbers of sense coils on FC-TPM when there are eddy current losses in the WPT coils. A 2-D axisymmetric FEM simulation in COMSOL was performed for two solid-wire WPT coils with the same dimensions as the hardware in Section VI. From (63) and (64), when eddy currents are significant, four sense coils are needed. Fig. 17 shows that with two-sense coils the errors are a considerable 0.66%. As the number of sense coils increases to four, the error reduces to a much smaller 1.6×10^{-9}%. Additional sense coils beyond four do not significantly improve the error for this case where the WPT coils are aligned.

In particular, this collection of four sense coils from the $N > 4$ sense coils results in ${}^N\text{C}_4$ independent transfer-power formulations, where we can extend the principle of FC-TPM over misalignment in Section IV-C to that which includes eddy

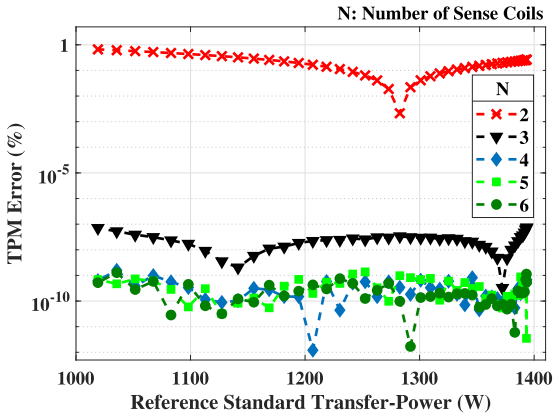

Fig. 17. FEM simulation was performed to show FC-TPM errors when eddy currents in the Tx and Rx coils are included.

current. By increasing the number of sense coils, the formulation in (65) can embed (52), ultimately resulting in a single set of geometric parameters that also include Rx coil misalignment together with the effects of eddy current.

The transfer-power at each misalignment x can be determined by

$$P_{\text{Transfer}}(x) = \sum_{i,j \in Q} \lambda_{ij}(x) \left\langle V_i(x), V_j(x) \right\rangle \tag{67}$$

where $\lambda_{ij}(x)$ can be approximated by an n^{th}-order polynomial

$$\lambda_{ij}(x) = a_n^{ij} x^n + a_{n-1}^{ij} x^{n-1} + \ldots + a_0^{ij}. \tag{68}$$

If N (> 4) sense coils are employed, there are $N_{\text{w}} (= {}^N\text{C}_4)$ independent transfer-power formulations for (67). Let $\mathcal{T}$ be a set of N sense coils, $\mathcal{T} = \{1, 2, \ldots, N\}$. $\mathcal{S}$ is a collection with lexical ordering of all subsets of $\mathcal{T}$ that consists of combinations of four sense coils; $\mathcal{S} = \{s_k | \, s_k \subset \mathcal{T}, \, \text{n}(s_k) = 4\}$, where $\text{n}(\mathcal{S}) = N_w$. Each independent formulation, a linear combination of pairwise-products of sense coil voltages from $s_k \in \mathcal{S}$, has a distinct set[11] $\lambda_{ij}^{(k)}$ of geometric parameters, where $k \in \{1, \ldots, N_w\}$.

The linear combination of the N_w transfer-power formulations with constant coefficients δ_k is then

$$\sum_{k=1}^{N_w} \delta_k P_{\text{Transfer}}(x) = \sum_{k=1}^{N_w} \sum_{\substack{i<j \\ i,j \in s_k}} \delta_k \lambda_{ij}^{(k)}(x) \left\langle V_i(x), V_j(x) \right\rangle \tag{69}$$

which approximates to a form like (52)

$$\begin{aligned} P_{\text{Transfer}} &= \sum_{i,j \in Q} \alpha_{ij} \left\langle V_i, V_j \right\rangle \\ Q &= \left\{ (i,j) \in \mathbb{N}^2 \,\middle|\, i \le N, j \le N, \text{ and } i < j \right\} \end{aligned} \tag{70}$$

[11]Note that the geometric parameters $\lambda_{ij}^{(k)}$ of the same pair of sense coils (i, j) for each subset s_k are distinct (e.g., $\lambda_{12}^{(1)} \neq \lambda_{12}^{(2)}$).

when δ_k is optimized by choosing the appropriate sizes and positions of the sense coils so that

$$\sum_{k=1}^{N_w} \delta_k \approx 1 \text{ and } \sum_{k\in\mathcal{G}_{ij}} \delta_k \lambda_{ij}^{(k)}(x) \approx \alpha_{ij} \tag{71}$$

where

$$\mathcal{G}_{ij} = \Big\{ \mathcal{K} \subset \{1,\ldots,N_w\} \,\big|\, k \in \mathcal{K} \text{ and } i,j \in s_k \Big\} \tag{72}$$

which has ${}^{(N-2)}\mathrm{C}_2$ elements; in other words, $\mathcal{G}_{ij}$ is a set of indices of s_k, which includes a specific sense coil pair i and j, noting that s_k is a set of combinations of four sense coils.[12]

The coefficients α_{ij} can be obtained from a least-squares optimization like (51)

$$\underset{\alpha_{ij}}{\text{minimize}} \quad \left\| P_{\text{Transfer}}(x) - \sum_{i,j\in Q} \alpha_{ij} \big\langle V_i(x), V_j(x) \big\rangle \right\|_2$$
$$\text{subject to } \alpha_{ij} \in \mathbb{R}. \tag{73}$$

The transfer-power can then be determined over the Rx coil misalignment by a single set of geometric parameters α_{ij}.

2) FEM Simulations of FC-TPM With Eddy Currents Over Multidimensional Variations: Misalignment, Litz-Wire Types, and Operating Frequencies: The principle that enables accurate FC-TPM over variations (e.g., misalignment) is the use of an overdetermined set of sense coils whose geometric parameters are such that the linear combination of the pairwise-products of their voltages are insensitive to errors from the variations. These had been presented in Sections IV-C2 and IV-E1.

The optimal linear coefficients are calibrated through the least-squares minimization of a calibration set, which is appropriately chosen over the range of variations of interest, as shown in (53)–(55). This formulation can be expanded to a multidimensional simultaneity of variations, such as having EVs (Rx coils) with different types of litz wires and operating frequencies. Calibration can be undertaken for both Tx and service station sense coils during manufacturing or when commissioned in the field for retrofits or repairs.[13]

Three-dimensional FEM simulations in COMSOL were performed to demonstrate accurate FC-TPM over multidimensional variations in the Rx coil, where the effects of eddy currents are included in the FEM simulation. The goal of the simulations is to confirm that transfer-power can be determined accurately using only a single set of geometric parameters regardless of those variations.

[12]For example, when $N = 6$ and $N_w = 15$, then $\mathcal{T} = \{1,2,3,4,5,6\}$ and $\mathcal{G}_{13} = \{1,2,3,7,8,9\}$, where s_k includes the particular sense coil pair $(i,j) = (1,3)$; $s_1 = \{1,2,3,4\}, s_2 = \{1,2,3,5\}, s_3 = \{1,2,3,6\}, s_7 = \{1,3,4,5\}, s_8 = \{1,3,4,6\}, s_9 = \{1,3,5,6\}$.

[13]From an arbitration perspective, with the inspection performed by an unbiased third party, the official trucks can have their sense coils, attached to the Rx coils to inspect the charging stations' metering accuracy. This is possible because the official trucks and sense coils are calibrated over Tx coil variations in standard laboratories. This is analogous to the *Weights and Measures Program* today in that officials bring trucks with *provers* that are carefully calibrated in standard laboratories [41], [42] to check the accuracy of gas dispensers.

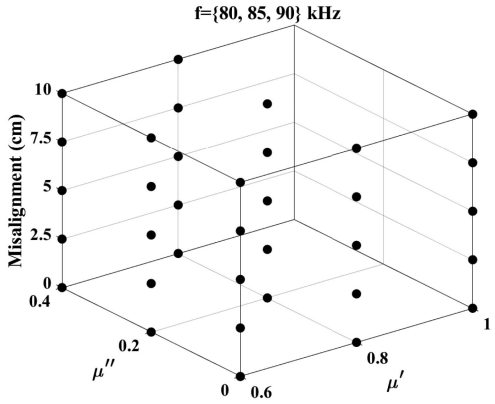

Fig. 18. Space of variations was created over Rx coil misalignment, complex permeability, and operating frequency for calibration and validation. A total of 105 data-points were used, where each point in the plot above represents a variation over three frequencies.

Notably, we show that using only a small number of wire types (including litz wire) for calibration, FC-TPM is accurate for a broad range of wire types that are not in the calibration set.

As illustrated in Fig. 18, FEM results consist of a total 105 data points, which are a combination of 1) Rx coil lateral misalignment: {0, 2.5, 5, 7.5, 10 cm}; 2) operating frequencies: {80, 85, 90 kHz}, which are within the mandated range of SAE J2954 [35]; and 3) seven complex permeabilities of different Rx windings: $\mu = 1$ (solid-wire) and $\mu' = \{0.8, 0.6\}$, $\mu'' = \{0, 0.2, 0.4\}$, where $\mu = \mu' - j\mu''$, which can model different bundles and strands of litz wire, using an equivalent complex permeability model [43], [44]; it is worth noting that the range of μ' and μ'' in Fig. 18 covers a broad range of wire types [43]–[45].

Fig. 19 shows an example configuration for a particular simulation iteration. To alleviate the computational complexity of an already intensive 3D simulation: 1) The Tx coil was modeled as a uniform surface current on a circular plane; 2) the Rx coil was a single-turn circular coil; 3) sense coil voltages were obtained postsimulation from the magnetic flux intersecting the coil area. The Rx coil radius was 12.5 cm, with a 5-mm diameter wire, specified in [35]. The Tx surface current's inner and outer radii were 5.5 and 12.5 cm, respectively. The air gap between the Rx coil and the Tx surface current was 10 cm. The sense coils were located on a plane 1.25 cm above the Tx surface current. The sense coil radii ranged from 18.25 to 3.25 cm decreasing at 1.5-cm intervals.

The accuracy of FC-TPM was verified using LOOCV. We used entire data subsets for a particular litz-wire type for validation. Specifically, in this particular variant of LOOCV, we iteratively left a particular litzwire type out of each calibration set and reserved it for validation to show that the calibration set can span the parameter variation space, hence maintaining FC-TPM accuracy over the broad range of litz-wire variations. In particular, the validation set consisted of 15 data points of a single wire type (i.e., a specific complex permeability), which were obtained from five misalignment values {0, 2.5, 5, 7.5, 10 cm}, and three frequency variations {80, 85, 90 kHz}. The remaining 90 data points consisting of 6 wire types, each with 15 variations, were the calibration set. The geometric parameters

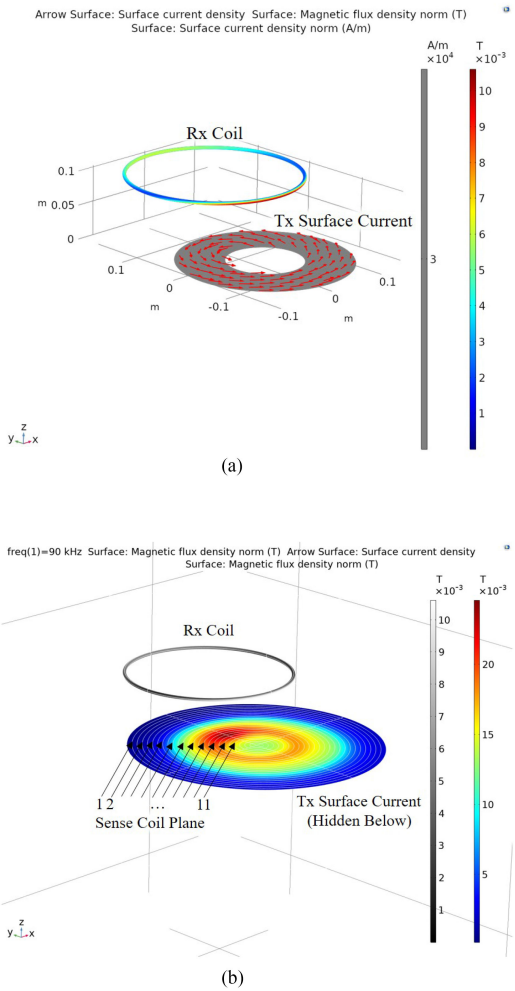

Fig. 19. 3-D FEM simulations were performed in COMSOL over a four-dimensional Rx coil variation $\{\mu', \mu'', x, f\}$. (a) Tx coil current was modeled as a uniform surface current. The Rx coil is a single-turn circular coil. (b) 11 different induced voltages on the sense coil plane were calculated from the magnetic field.

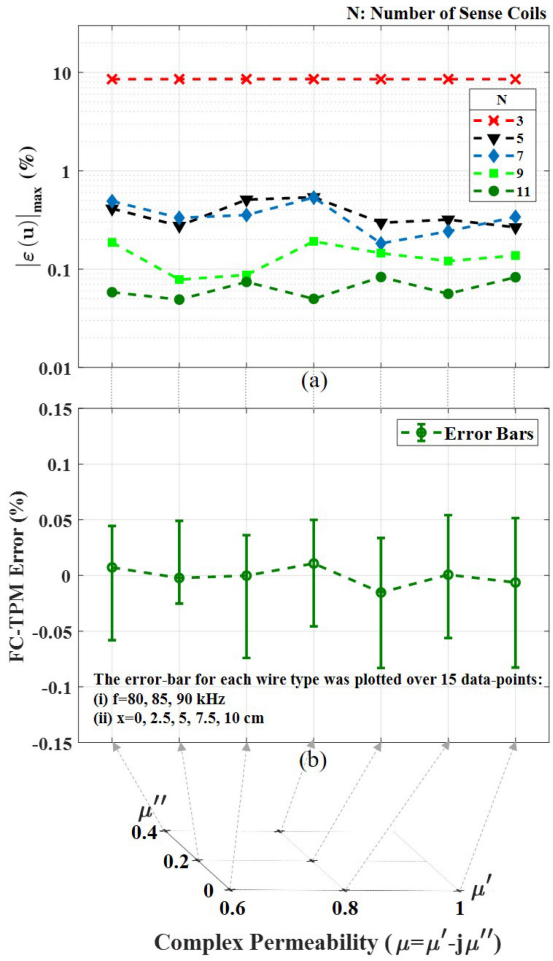

Fig. 20. (a) Worst-case absolute error percentage for each type of wire (represented by the complex permeability) as the number of sense coils is increased. (b) The spread in error using 11 sense coils for each type of wire over both frequency and misalignment variation.

α_{ij} were calculated at each LOOCV iteration for the calibration set using (53)–(57).

FC-TPM errors were calculated for each validation point. Using α_{ij} with 11 sense coil voltages, the transfer-power was determined for each point using (70) and the error was calculated with (58), where the reference standard transfer-power was calculated from (25). Fig. 20(a) shows the worst-case absolute error percentage, as defined in (61), for each type of wire (represented by the complex permeability) as the number of sense coils is increased, where $\mathbf{u}_k = [\mu \quad x_k \quad f_k]$. Eleven sense coils reduced the error to below 0.1%. Fig. 20(b) shows the spread in error using 11 sense coils for each type of wire over frequency and misalignment variation; the errors were ranged from -0.083% to $+0.054\%$.

Future work will include validating other variations including environmental influences for the one-time calibration of FC-TPM: 1) Variations in coil winding methods (e.g., concentrated, solenoidal, and spiral); 2) Tx coil variations in wire type and winding method; and 3) optimization of sense coil placement and size. Note that unacceptable environmental influences including hazardous objects or defects can be detected and power transfer stopped; for example, a foreign object, which is a fire hazard, can be detected by the FC-TPM system [46].

V. Electromagnetically Thin and Physically Flat Sense Coils

Effective sensors should not affect that which it is measuring nor should it negatively impact the primary mission of charging vehicles. In this section, we show how the sense coils for FC-TPM can be constructed so they are a minimal electromagnetic perturbation and be designed to be below the pavement. Using high fidelity FEM using COMSOL, we show that the eddy current losses dissipated in the sense coils are insignificant and hence electromagnetically "thin." We then show through a multiobjective optimization that a low-profile coplanar sense coil geometry, in other words "flat," has a comparable performance to other optimized configurations.

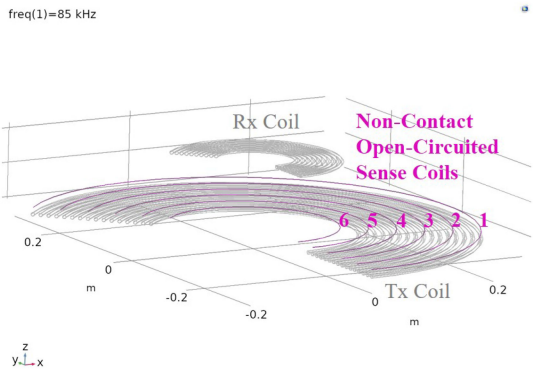

Fig. 21. 2-D axisymmetric FEM simulation for analyzing eddy current losses in the sense coils. The coplanar sense coils were open-circuited and single-turn.

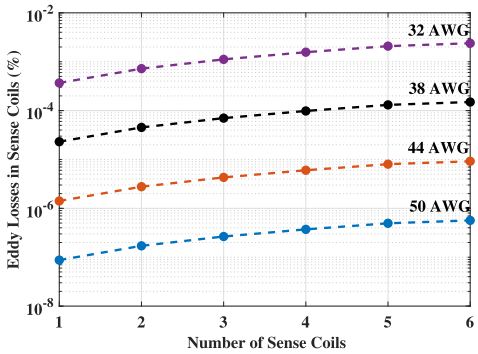

Fig. 22. Efficiency loss from eddy currents in the sense coils: wire diameter and number of sense coils were varied.

A. Eddy Current Losses Dissipated in Open-Circuited Sense Coils

The sense coils are supplemental to a WPT charging system and should neither impact the efficiency nor perturb the electromagnetic fields. The sense coils are open-circuited, and hence do not carry terminal current, so there is no ohmic loss. A potential loss mechanism may be the eddy currents induced by the time-varying magnetic fields generated by the Tx and Rx coil currents; however, these losses are negligible when the sense coils are very thin; 50-AWG (0.025-mm diameter) coaxial cable is available commercially.

Eddy current losses in the sense coils were analyzed through 2D axisymmetric FEM simulations with an extremely fine mesh in COMSOL. Open-circuited single-turn sense coils were placed 1 cm above the Tx coil, as shown in Fig. 21, where the Tx and Rx coils were multiturn concentric circular coils, used in Section III-C for the WPT2/Z1 class. Eddy current losses were calculated for different numbers (one to six) and diameters (32 to 50 AWG, at 6-AWG intervals) of sense coils.

Fig. 22 shows the efficiency loss from eddy currents in the sense coils. The diameter of the sense coils, which scales the loss as approximately cubic, is the dominant factor; whereas, the number of sense coils scale the loss linearly. Using commercially available 50-AWG coaxial cable, the eddy current loss only contributes less than $10^{-6}\%$ efficiency loss according to the results from these high fidelity electromagnetic FEM simulations.

B. Physically Flat Sense Coils: Performance Comparisons With Other Configurations

Physically flat sense coils are unobtrusive and can be installed above the transmitter coil and below the pavement if needed. In this section, we show that coplanar sense coils have comparable performance with other configurations. We use Monte Carlo methods to evaluate three performance metrics: 1) Model matching; 2) information diversity; and 3) detectability. Pareto frontiers from a multiobjective optimization [47] of each configuration is used for comparison. The Pareto frontier is the best performance set for a particular configuration. In other words, by comparing Pareto frontiers, one compares the best cases of each configuration. Specifically, we compare coaxial sense coils that are restricted to the same plane, i.e., flat/coplanar, with those that are only restricted coaxially, but otherwise unrestricted.

A multiobjective optimization problem was formulated from the weighted sum of three penalty functions [48]

$$\begin{aligned} \underset{\mathbf{r},\mathbf{d}}{\text{minimize}}\ & \lambda_1 p_1 + \lambda_2 p_2 + \lambda_3 p_3 \\ \text{subject to}\ & \mathbf{r} = [r_1\ r_2\ \cdots\ r_N] \\ & \mathbf{d} = [d_{T:1}\ d_{T:2}\ \cdots\ d_{T:N}] \\ & \hat{R}_{\min} \le \tfrac{r_i}{r_T} \le \hat{R}_{\max} \\ & \hat{d}_{\min} \le \tfrac{d_{T:i}}{d_{T:R}} \le \hat{d}_{\max} \\ & 0 \le \lambda_1, \lambda_2, \lambda_3 \le 1 \\ & \lambda_1 + \lambda_2 + \lambda_3 = 1. \end{aligned} \tag{74}$$

Each penalty function (p_1, p_2, and p_3) ranges from zero to one, normalized over the Monte Carlo data from all the comparison configurations.

Together, these penalty functions represent a tradeoff between 1) errors from mismatch between the sense coils and the models used for TPM reconstruction; 2) sensitivity to measurement errors and noise in calibration; and 3) signal-to-noise ratio in the sense coil measurement. The sense coil parameters that determine the penalty functions include the sense coil radii r_i and the vertical distance from the Tx coil to the sense coils $d_{T:i}$ for N sense coils, where $i \in \{1, \ldots, N\}$. $\hat{R}_{\min}$ and $\hat{R}_{\max}$ represent range of sense coil radii normalized to the Tx coil radius r_T. $\hat{d}_{\min}$ and $\hat{d}_{\max}$ are the sense coil positions above the Tx coil normalized to the distance between the Tx and Rx coils $d_{T:R}$. λ_i are the weights for the penalty functions.

The analysis and computation are tractable when eddy currents are neglected and only the principal transfer-power is used. The following subsections detail each penalty function and show the results of the comparison.

1) Model Matching: The errors in FC-TPM can be made small and insensitive to variation when the sizes and positions of the sense coils are chosen so that the deviation from the models used in reconstruction is small. p_1 penalizes model mismatch.

For example, when the mutual inductance from the Tx coil to the Rx coil varies so it is predominantly quadratic over Rx coil misalignment, placing the sense coils close to the Tx coil makes the corresponding geometric parameters also predominantly quadratic as discussed in Section IV-C. In this case, p_1 penalizes the nonquadratic deviations over Rx coil misalignment in the

sense-to-Rx coil mutual inductance. The penalty function can be evaluated using Grover's expression for mutual inductance [37] with the quadratic model presented in Section IV-C1

$$p_1 = \frac{q_1(\mathbf{r},\mathbf{d}) - \min\limits_{\mathbf{r},\mathbf{d}} q_1(\mathbf{r},\mathbf{d})}{\max\limits_{\mathbf{r},\mathbf{d}} q_1(\mathbf{r},\mathbf{d}) - \min\limits_{\mathbf{r},\mathbf{d}} q_1(\mathbf{r},\mathbf{d})} \tag{75}$$

where

$$q_1(\mathbf{r},\mathbf{d}) = \log\left(\sum_{i\in\{1,\ldots,N\}} \frac{\left\| M_{R:i}(r_i, d_{T:i}, x) - \widehat{M}_{R:i}(r_i, d_{T:i}, x)\right\|_2^2}{\|M_{R:i}(r_i, d_{T:i}, x)\|_2^2}\right). \tag{76}$$

$M_{R:i}(r_i, d_{T:i}, x)$ is the mutual inductance between the sense coil and Rx coil which is calculated from the Grover; $\widehat{M}_{R:i}(r_i, d_{T:i}, x)$ is the mutual inductance from the quadratic model; r_i is the radius of the i^{th} sense coil; $d_{T:i}$ is the distance between the i^{th} sense coil and the Tx coil; x is the Rx coil misalignment; and $\|\cdot\|_2$ is the $l_2[0, x_{\max}]$ norm over a closed interval and a sampling of the continuous functional $\widehat{M}_{R:i}(\cdot,\cdot,x)$ and its corresponding discrete data sequence $\widehat{M}_{R:i}(\cdot,\cdot,x[n])$.

2) Information Diversity: Overlapping information in the least-squares minimization of the data matrix of sense coil voltages $\mathbf{W}$, defined in (53), results in poor matrix conditioning and consequently sensitivity to noise and measurement error.

In the calibration of FC-TPM, least-squares minimization is performed, where $\mathbf{W}$ is inverted in (57). When the sense coil voltages are independent, the calibration is robust to measurement noise. Hence, sense coils are chosen and arranged to minimize overlapping information in the voltages.

Mutual inductance can be used as a proxy for information overlap among sense coil voltages because mutual inductance is a measure of the shared magnetic flux between two sense coils and hence information. Large mutual inductance between two sense coils may physically mean that they are similar in size and/or proximal.

p_2 penalizes information similarity. It is formulated by normalizing and taking the logarithm of the sum of squares of the mutual inductances between sense coil pairs. p_2 ranges from from 0 to 1: "0" indicates that all pairs of sense coils have maximum independence given the optimization constraints; "1" indicates the worst case among all sense coil configurations in all the comparison cases

$$p_2 = \frac{q_2(\mathbf{r},\mathbf{d}) - \min\limits_{\mathbf{r},\mathbf{d}} q_2(\mathbf{r},\mathbf{d})}{\max\limits_{\mathbf{r},\mathbf{d}} q_2(\mathbf{r},\mathbf{d}) - \min\limits_{\mathbf{r},\mathbf{d}} q_2(\mathbf{r},\mathbf{d})} \tag{77}$$

where

$$q_2(\mathbf{r},\mathbf{d}) = \log\left(\sum_{i,j\in Q} M_{i:j}^2(r_i, d_{T:i}, r_j, d_{T:j})\right). \tag{78}$$

$M_{i:j}(r_i, d_{T:i}, r_j, d_{T:j})$ is the mutual inductance between the i^{th} and j^{th} sense coil. The mutual inductance increases as the two sense coils are closer to each other $d_{T:i} \to d_{T:j}$ and have similar radii $r_i \to r_j$, which penalizes the lack of information diversity.

3) Detectability: The detectability is the ability of a particular FC-TPM configuration to resolve a change in the transfer-power from a change in either the Tx or Rx coil current. This is equivalent to the signal-to-noise ratio (SNR) of the different sense coil voltages from the change in the Tx/Rx coil current to the instrumentation noise referred to the sense-coil voltage. The mutual inductances between the sense coils and the Tx coil $M_{T:i}$ or Rx coil $M_{R:i}$, determine the sense coil voltages from the Tx and Rx coil currents. p_3 penalizes poor SNR in the sense coil configuration; we assume that a change in Tx current is just as likely as a change in Rx current.

$$p_3 = \frac{q_3(\mathbf{r},\mathbf{d}) - \min\limits_{\mathbf{r},\mathbf{d}} q_3(\mathbf{r},\mathbf{d})}{\max\limits_{\mathbf{r},\mathbf{d}} q_3(\mathbf{r},\mathbf{d}) - \min\limits_{\mathbf{r},\mathbf{d}} q_3(\mathbf{r},\mathbf{d})} \tag{79}$$

where

$$q_3(\mathbf{r},\mathbf{d}) = \sum_{i\in\{1,\ldots,N\}} \frac{1}{M_{T:i}^2(r_i, d_{T:i})} + \sum_{i\in\{1,\ldots,N\}} \frac{1}{M_{R:i}^2(r_i, d_{T:i})}. \tag{80}$$

Note that $M_{T:i}(r_i, d_{T:i})$ is the mutual inductance between the Tx coil and the i^{th} sense coil; $M_{R:i}(r_i, d_{T:i})$ is the mutual inductance between the Rx coil and the ith sense coil. We choose the Tx, Rx, and sense coils to be aligned for tractability. The total SNR is the harmonic mean of the SNR of each sense coil. p_3 penalizes overly large- or small-sized sense coils, or positions which are far from both the Tx and Rx coils.

4) Comparison Results: Good sense coils have: 1) small quadratic approximation error for the mutual inductance over Rx coil misalignment; 2) diverse information, which minimizes the least-squares errors during calibration; and 3) good SNR in the sense coil voltages for accurate transfer-power reconstruction. It is worth noting that the three penalty functions are counteractive vis-à-vis the sense coil positions and sizes. Based on observations, 1) p_1 is smaller when the sense coils are all near the Tx coil; 2) p_2 is smaller when the sense coils are far apart and have different sizes; and 3) p_3 is smaller when the sense coils are of similar size to and in joint proximity to the Tx and Rx coils. The performance metrics of coplanar sense coil configurations are compared to other sense coil geometries with fewer restrictions for $N = 6$ sense coils. Design classes such as sense coil configurations should be compared by their optimal designs on Pareto frontiers. The class of coplanar sense coil configurations (i) is topologically defined by the constraints that the sense coils share the same axis (coaxial) and lie on the same plane

$$d_{T:1} = d_{T:2} = \cdots = d_{T:6}. \tag{81}$$

Sense coil configuration class (ii) is topologically constrained only to be coaxial.

A numerical comparison was performed using Monte Carlo methods together with Manhattan sampling[14] using identical Tx

[14]The simulation uses the Manhattan sampling [49]. The search space $(\frac{r_i}{r_T}, \frac{d_{T:i}}{d_{T:R}})$ is uniformly partitioned into 3×3 rectangular regions. These 9 rectangular regions are exhaustively travelled. The sampling follows the uniform distribution inside each rectangular region.

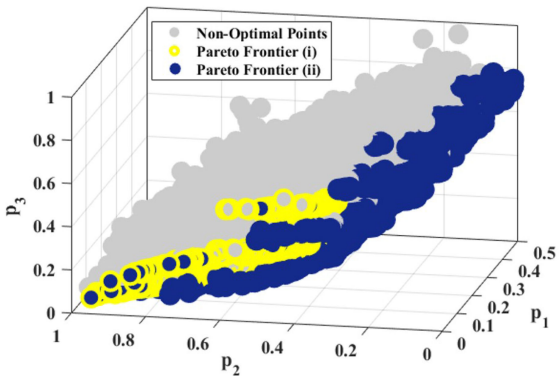

Fig. 23. Comparison results between coaxial-coplanar and coaxial-unrestricted sense coils. The yellow shows the Pareto frontier (optimal points) when sense coils are restricted to coplanar configurations. The blue shows the Pareto frontier (optimal points) when there is no restriction on the coaxial sense coil placement. The gray shows some nonoptimal sense coil geometries.

and Rx coil radii ($r_T = r_R = 22.5$ cm) separated by $d_{T:R} = 20$ cm, which corresponds to the hardware in Section VI. The addition geometric constraints are $\hat{R}_{\min} = 0.44$, $\hat{R}_{\max} = 1.78$, $\hat{d}_{\min} = 0.05$, and $\hat{d}_{\max} = 0.95$. This search space is large enough to cover the sense-coil geometries which are physically realizable.[15]

We swept λ_2 and λ_3, and solve (74) to obtain the optimal points $r_i^*(\lambda_2, \lambda_3)$ and $d_{T:i}^*(\lambda_2, \lambda_3)$ on the Pareto frontiers. The optimal points for the two sense coil configuration classes, shown in Fig. 23, form surfaces which are the Pareto frontiers for each of the multiobjective optimizations. The hollow yellow circles correspond to the Pareto frontier for coplanar sense coil configurations (i); the solid blue circles correspond to less restrictive sense coil configurations (ii); and the solid gray circles correspond to nonoptimal points. These are an illustrative sampling of the 4 billion points tested. The Pareto frontiers largely overlap, which indicates that coplanar sense coils have comparable performance to less restrictive sense coil geometries.

VI. Hardware Results

We demonstrated FC-TPM in hardware with a 1-kW wireless charging system that operates at 85 kHz using 270 strands of 38-AWG (0.101-mm diameter) litz wire for the Tx and Rx coils. The Tx and Rx coils are each ten-turn solenoids, whose diameter is 45 cm with an air gap ($d_{T:R}$) of 20 cm between the coils. Each of the FC-TPM sense coils are single-turn, open-circuited, and placed on the same plane 2.5 cm above the Tx coil ($d_{T:i}$), as shown in Fig. 24. A very thin coaxial cable, 42 AWG (0.06335-mm outer diameter), was used for each single-turn sense coil winding. The coaxial cable was configured so the outer braid acted as an electrostatic shield from the high voltage Tx and Rx windings[16] [50].

[15]To verify, sense coil geometries outside of this search space were sampled in Monte Carlo simulations; the results do not belong to the Pareto frontier.

[16]Only one terminal of the shield was grounded to preclude a shorted turn.

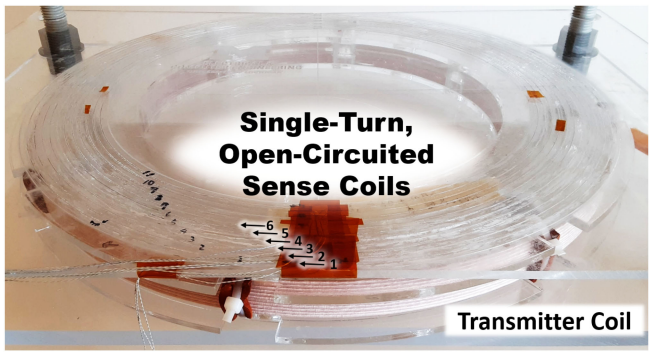

Fig. 24. Sense coils are in the flat plane above the Tx coil.

TABLE III
WPT Coil Specifications

Parameters	Value	Parameters	Value
r_T, r_R	22.5 cm	r_i	22.5 - 0.5 $\cdot (i-1)$ cm
L_T	108.8 μH	$d_{T:R}$	20 cm
L_R	108.4 μH	$d_{T:i}$	2.5 cm

r_T, r_R, r_i: The radii of the Tx, Rx, and sense coils
L_T, L_R: The self-inductance of the Tx (Rx) coil
$d_{T:R}$: The distance between the Tx and Rx coil (center to center)
$d_{T:i}$: The distance between the Tx (center) and sense coils
i: The index of the sense coils

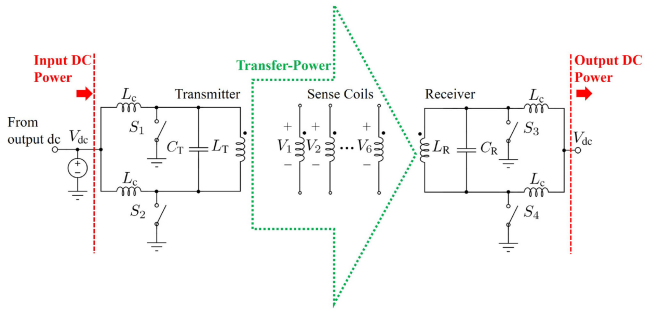

Fig. 25. Current-mode class D wireless power transfer system with open-circuited FC-TPM sense coils. DC current was recirculated with the input and output voltage held fixed.

Table III presents the specifications of the Tx, Rx, and sense coils.[17]

The Tx and Rx coil were driven by identical current-mode class D (CMCD) converters [51]–[53]; the power level from the Tx to the Rx coil was adjusted by changing the phase angle of the gate signals, hence changing the corresponding WPT coil voltages and currents [51]. The dc output of the receiver was recirculated to the input of the transmitter, with a single dc power supply V_{dc} holding the voltage of the shared dc node fixed while supplying the power loss. The CMCD WPT circuit configuration is shown in Fig. 25; one of the CMCD printed circuit boards is shown in Fig. 26. 1.2-kV SiC MOSFETs were used to block the 1-kV drain voltages. Table IV lists the components specifications. The resonant capacitors were chosen to carry the nearly 12-A_{rms} current. Fig. 27 shows the Tx and Rx coil voltages and

[17]The self-inductances of the Tx and Rx coil were measured by an Agilent E4980 LCR meter.

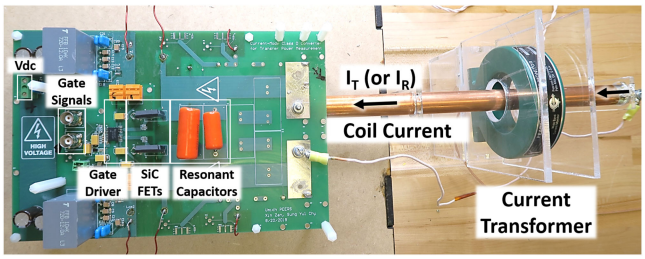

Fig. 26. 1-kW current-mode class D converters were designed to drive the WPT coils. A Pearson current transformer (CT) was used to measure the Tx and Rx coil current using a rigid copper tube at the center of the CT to maintain accuracy.

TABLE IV
CURRENT-MODE CLASS D CONVERTERS COMPONENTS

Parameters	Value	Parameters	Value
SiC MOSFET	C3M0075120K	Resonant Capacitors	32 nF
Gate Driver	UCC21530	Switching Frequency	85 kHz

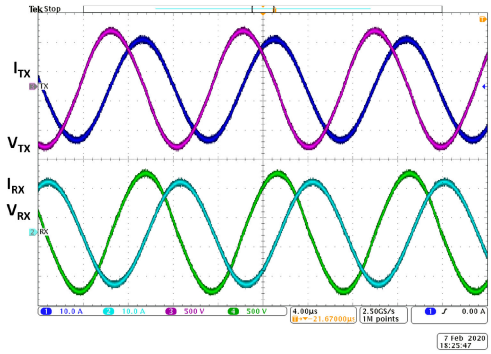

Fig. 27. Tx and Rx coil voltages and currents driven by CMCD converters.

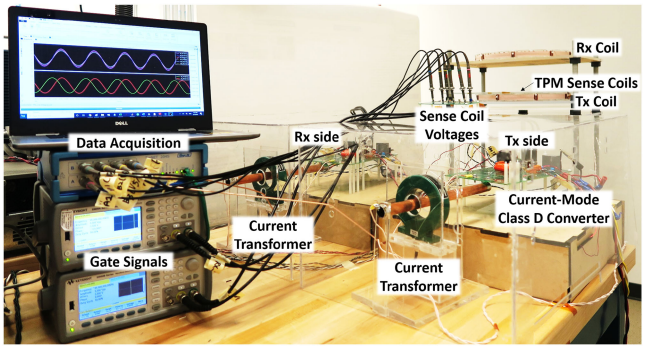

Fig. 28. Faraday coil transfer-power measurement (FC-TPM) test system.

currents that demonstrate kW-level WPT, driven by two CMCD converters. Note that V_{TX} and $-I_{RX}$ (current into the receiver) are nearly in phase to deliver real power from the transmitter to the receiver.

The FC-TPM system was built as shown in Fig. 28. Current transformers (Pearson Model 110) were used to measure the Tx and Rx coil currents. The Tx and Rx coil current, and sense coil voltage data were each 16 megasample recordings on an Elsys TraNET 204E with a TCPE-8016-4S data acquisition system at

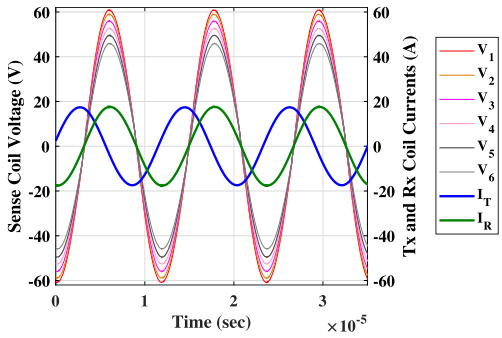

Fig. 29. Sense coil voltages and Tx, Rx coil currents were measured and recorded by a 20 Msamples/s, 16-bit data acquisition system for FC-TPM.

20 Msamples/s, 16-bit resolution; Fig. 29 shows the recorded coil currents and sense coil voltages.

A. FC-TPM With Two Sense Coils

We show FC-TPM can be demonstrated in hardware by confirming that the transfer-power can be accurately determined by using sense coil voltages together with calibrated geometric parameters. Using aligned and stationary Tx and Rx coils, we examined the accuracy from using only two sense coils (22.5 and 17.5-cm radii).

Only one single geometric parameter (42) needed to be calibrated using the least-squares minimization in Section IV-D performed over load. The data space spanned a variation in transfer-power by sweeping the phase difference between Tx and Rx coil currents at constant amplitude.[18] The reference standard transfer-power was measured simultaneously as described in Appendix E.

LOOCV was used to validate the accuracy of FC-TPM; the geometric parameter was determined by the calibration set (9 data points), the transfer-power of the validation set (1 data point) was determined from (41), and the reconstruction errors in (58) were calculated. The FC-TPM errors are shown in Fig. 30(b). The hardware errors ranged from -0.009% to 0.015%.

By using the appropriate litz wire in our WPT coils, eddy currents can be made negligible. In Fig. 30, two sense coils (22.5 and 17.5-cm radii) were used for the FC-TPM of aligned WPT coils described above. Calibrated principal transfer-power using (40) is shown for solid wire in COMSOL FEM simulation in Fig. 30(a) and litz wire in hardware in Fig. 30(b). From Section IV-E, using two sense coils for FC-TPM when there are eddy current losses in the WPT coils result in nonnegligible errors. This is manifested in the solid wire in Fig. 30(a) as a systematic error with increasing transfer-power; this systematic error can be interpreted as the error from the excess loss imposed by the additional eddy current winding in the transformer model in Section IV-E1. Fig. 30(b) shows errors that can be attributed in part to measurement and reference standard calibration that includes sensor error, noise, and digital quantization.

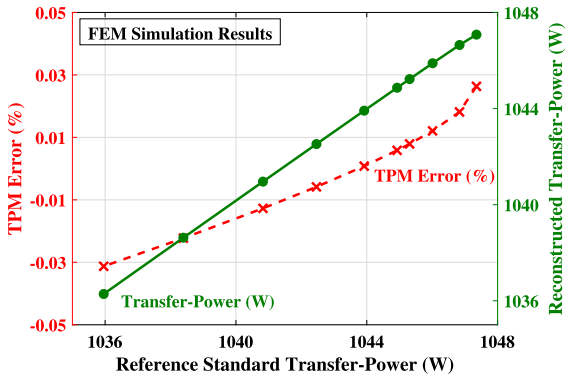

(a)

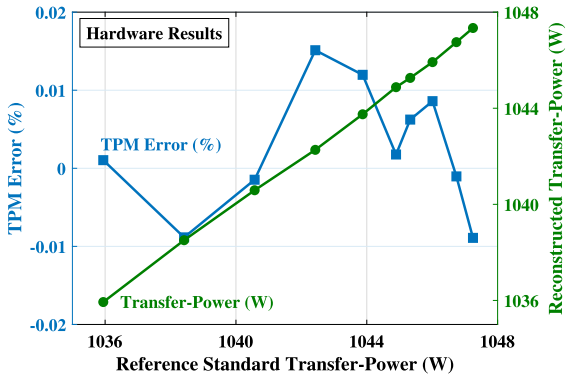

(b)

Fig. 30. Solid wire and litz wire are compared for Tx and Rx coils using FEM and hardware for principal FC-TPM. (a) COMSOL FEM results for solid-wire Tx and Rx coils. (b) Hardware results of FC-TPM for an aligned Rx coil. Reconstructed transfer-power through FC-TPM is compared with the reference standard transfer-power at each validation point.

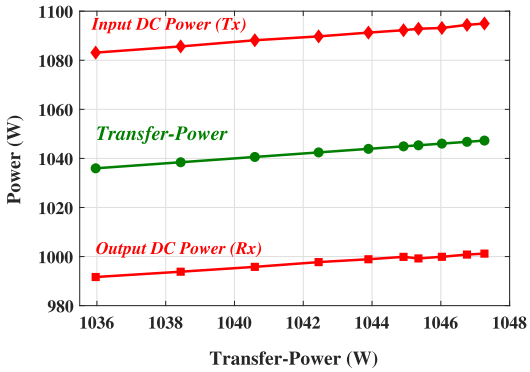

Fig. 31. Transfer-power is compared to dc input and output power measured at the electrical terminals. Terminal power is fundamentally not the same as transfer-power.

The transfer-power is also compared in Fig. 31 to the input and output dc power to highlight and demonstrate the principle that measuring transfer-power disaggregates the Tx and Rx losses to enable fair metering. FC-TPM was also demonstrated over a wide range of power levels as illustrated in Fig. 32, where the error is less than 0.1% (-0.011% to 0.096%) from 60 W to 1 kW.

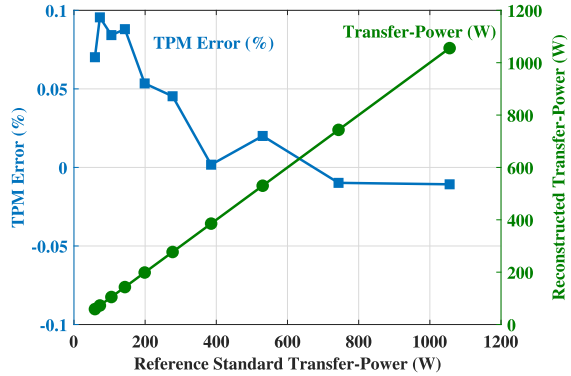

Fig. 32. FC-TPM was demonstrated in hardware over a wide range of power levels.

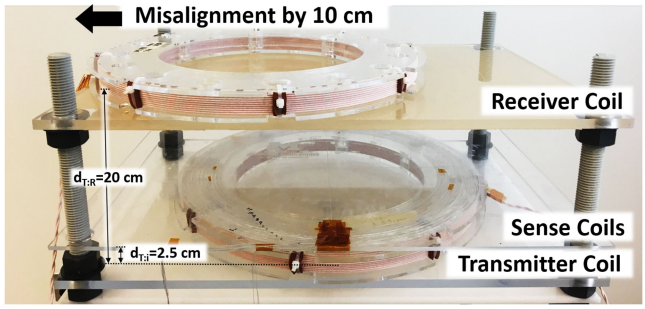

Fig. 33. Faraday coil transfer-power measurement was demonstrated over SAE J2954 Rx coil misalignment.

B. FC-TPM Over Misalignment

We demonstrated FC-TPM over Rx coil misalignment using six sense coils (radii from 20 to 22.5 cm at 0.5-cm intervals). The Rx coil was misaligned[19] by up to 10 cm (6 data points: 0 to 10 cm at 2-cm intervals), as shown in Fig. 33. The data matrix $\mathbf{W}$ and vector $\mathbf{p}$ spans six misalignment values and ten Tx-Rx coil current phase differences to calibrate the geometric parameters α_{ij} according to (57). The percentage FC-TPM errors ϵ at each validation data point were calculated with (58) and plotted in Fig. 34. The error bars represent the range of errors at each misalignment point. The errors ranged from -0.087% to 0.07% and were very nearly consistent, demonstrating accurate FC-TPM over misalignment. It is worth noting that the explicit measurement of misalignment was not needed either for calibration or transfer-power estimation because the sense coil voltages and the constant geometric parameters encapsulate all the necessary information. The transfer-power is compared to the input and output dc power over misalignment in Table V and Fig. 35.

The dependence of FC-TPM errors to different numbers (from two to six) of sense coils were investigated. Fig. 36 shows the

[18]We varied the phase of the Rx coil drain voltages over 10 data points, resulting in changes in the coil currents, which corresponds to different equivalent output load resistances in Rx.

[19]Specified in SAE J2954 [35].

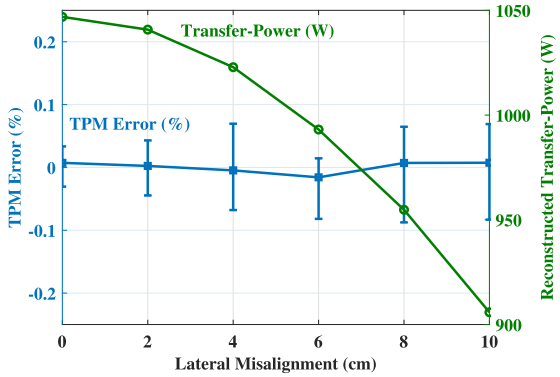

Fig. 34. Hardware results for FC-TPM errors over Rx coil misalignment. The transfer-power can be determined accurately despite misalignment.

TABLE V
INPUT,TRANSFER, AND OUTPUT POWER OVER MISALIGNMENT

Misalignment (cm)	Input DC Power (W)	Transfer-Power (W)	Output DC Power (W)
0	1,095	1,047	1,001
2	1,088	1,041	995.5
4	1,070	1,022	977.4
6	1,040	993.1	947.7
8	1,001	954.8	909.1
10	952.1	906.0	859.2

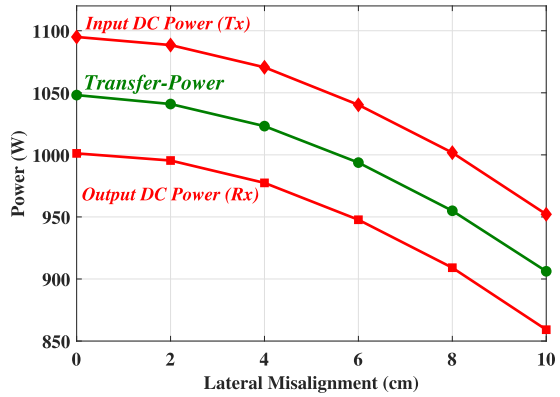

Fig. 35. Hardware results: FC-TPM disaggregates the Tx and Rx losses over misalignment.

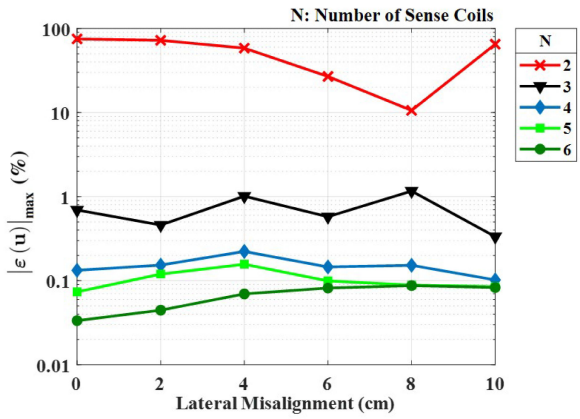

Fig. 36. Hardware results: FC-TPM accuracy was verified for different numbers of sense coils. An increasing number of sense coils results in more information and therefore better accuracy.

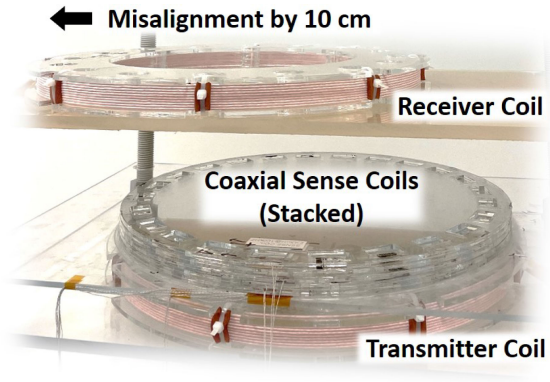

Fig. 37. FC-TPM was demonstrated over Rx coil misalignment when coaxially stacked sense coils were used.

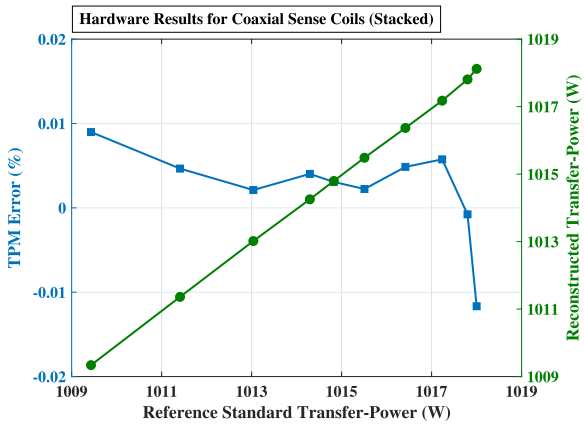

Fig. 38. Hardware results for FC-TPM errors for an aligned Rx coil when the coaxial sense coils are vertically stacked. The performance is comparable to that of the coplanar sense coils.

worst-case absolute error percentage of FC-TPM at 1 kW, as defined in (61), of ten data point variations in Tx-Rx coil current phase difference at each misalignment point. The greater the number of sense coils, the smaller the FC-TPM errors, which is expected because more information is available to determine the transfer-power over misalignment.

C. Performance Comparison to Coaxially Stacked Sense Coils

We replaced the coplanar sense coils with coaxially stacked sense coils, as illustrated in Fig. 37, to show the comparable performance of FC-TPM using the two different sense coil configurations. First, we examined the accuracy of using two 22.5-cm radii sense coils, which are coaxially stacked 3.5 and 7.5 cm above the Tx coil, respectively. A total of ten data points using different equivalent output load resistances were validated, and Fig. 38 shows the hardware results; the FC-TPM errors ranged from -0.011% to 0.009%, which are comparable to the errors from using coplanar sense coils in Fig. 30(b).

We also demonstrated FC-TPM over Rx coil misalignment using six coaxially stacked sense coils (vertical distances above the Tx coil from 3 to 5.5 cm at 0.5-cm intervals), as shown in Fig. 37. Fig. 39 shows the percentage error, where the error bars represent the range of error at each misalignment point. The

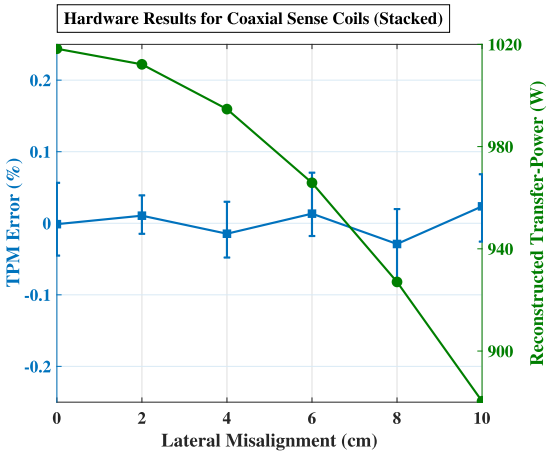

Fig. 39. Hardware results for FC-TPM errors over Rx coil misalignment when the coaxial sense coils are vertically stacked. The performance is comparable to that of the coplanar sense coils.

errors ranged from -0.082% to 0.071%, which are comparable to the errors from using coplanar sense coils in Fig. 34.

D. Future Implementation

Sense coils are the primary sensors, single-turn and open-circuited; conductors can be direct-printed on an insulator like FR4, and thus, inherently inexpensive and straightforward to manufacture. Commercial off-the-shelf analog-to-digital converters can be used to measure the sense coil voltages, and a field-programmable gate array can process the data. A digital signal processing microcontroller can control the measurements and communicate with other devices. The hardware cost is expected to be similar to typical measurement systems [22], [54]–[56] including those planned for metering in the NIST-sponsored U.S. National Work Group (USNWG) on Measuring Systems for Electric Vehicle Fueling and Submetering (EVF&S) [57]. Furthermore, the noncontact method of FC-TPM has an additional cost savings in that the high voltage safety and insulation that is required for typical terminal voltage and power measurements is not needed.

VII. Conclusion

In this article, FC-TPM was introduced, analyzed, and demonstrated. Implementation on a 1-kW WPT hardware system shows better than 0.1% accuracy over a wide range of transfer-power, confirming fair and accurate metering of WPT, which to our knowledge, is a first among methods in EV charging.

Transfer-power was shown to be fundamentally derived from the Poynting vector, which is the power purely dispensed from the Tx to the Rx coil through the intervening space. Transfer-power is profoundly different from the black box notion of a coil's electrical terminal power, which contains commingled losses from the Tx and Rx coils. Transfer-power ensures fair metering by attributing losses equitably between the charging station (Tx) and electric vehicle (Rx) based on the location of the heat dissipation as a demarcation.

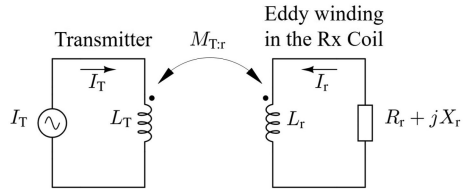

Fig. 40. Equivalent circuit for the winding model of the eddy current; the Tx coil and eddy current winding in the Rx coil are magnetically coupled.

Electromagnetically thin and physically flat, noncontact open-circuited sense coils are employed using only the sense coil voltages to accurately determine the transfer-power, even over misalignment. FC-TPM does not need misalignment measurements. Future research includes accurate FC-TPM over all multidimensional variations, including other types of charging geometries.

Economic decisions by stakeholders will require fine-grained information about efficiency and energy consumption. This is evidenced by growing efforts to standardize the accurate metering of EV charging. Ultimately, this will incentivize a continuing investment in technology and innovation.

Appendix A
Derivation of Eddy Current Loss in the Rx Coil

The eddy currents in the coils can be modeled as a transformer winding [33], [34]. In this Appendix, the eddy current in the Rx coil I_r, created by the Tx coil current I_T, is modeled as a winding to represent the eddy current loss in terms of the Tx coil current and effective resistance $R_{T:r}$. The equivalent circuit is shown in Fig. 40, resulting in the expression

$$-j\omega L_r I_r - j\omega M_{T:r} I_T = (R_r + jXr) I_r \tag{82}$$

where $M_{T:r}$ is the mutual inductance between the Tx coil and Rx coil's eddy current winding; R_r and X_r are the equivalent resistance and reactance in the winding.

From (82), the eddy current I_r can be represented in terms of the Tx current I_T

$$I_r = \frac{j\omega M_{T:r}}{-(R_r + jX_r + j\omega L_r)} I_T. \tag{83}$$

Transfer-power between two coils was defined in (12). The eddy current losses $P_{\text{Loss,eddy(Rx)}}$ can also be represented as a transfer-power

$$P_{\text{Loss,eddy(Rx)}} = \text{Re}\left\{j\omega M_{T:r} I_r I_T^*\right\}. \tag{84}$$

Note that the eddy current loss is the power that is transferred from the Tx coil to the eddy winding. The eddy current loss can also be found from (82) as the real power, dissipated by R_r

$$R_r \,\text{Re}\left\{I_r I_r^*\right\} = \text{Re}\left\{j\omega M_{T:r} I_r I_T^*\right\} \tag{85}$$

confirming (84).

Combining (83) and (84), the eddy current losses can be represented by

$$\begin{aligned} P_{\text{Loss,eddy(Rx)}} &= \text{Re}\left\{R_{T:r} I_T I_T^*\right\} + \text{Re}\left\{j\omega X_{T:r} I_T I_T^*\right\} \\ &= \text{Re}\left\{I_T I_T^*\right\} R_{T:r} \end{aligned} \tag{86}$$

where

$$R_{T:r} = \frac{\omega^2 M_{T:r}^2 R_r}{R_r^2 + (X_r + \omega L_r)^2} \tag{87}$$

$$X_{T:r} = \frac{\omega M_{T:r}^2 (X_r + \omega L_r)}{R_r^2 + (X_r + \omega L_r)^2}. \tag{88}$$

The eddy current loss is represented in terms of the Tx coil current I_T and the effective resistance $R_{T:r}$.

The Tx coil terminal-voltages V_T can be derived using (15), (83), (87), and (88)

$$\begin{aligned} V_T &= j\omega L_T I_T + j\omega M_{R:T} I_R + j\omega M_{T:r} I_r + R_T (I_T + \gamma_R I_R) \\ &= j\omega (L_T - X_{T:r}) I_T + j\omega M_{R:T} I_R + R_T (I_T + \gamma_R I_R) \\ &\quad + R_{T:r} I_T. \end{aligned} \tag{89}$$

Similarly, the Rx coil terminal voltage V_R can represented by

$$\begin{aligned} V_R &= j\omega (L_R - X_{R:t}) I_R + j\omega M_{T:R} I_T \\ &\quad + R_R (I_R + \gamma_T I_T) + R_{R:t} I_R. \end{aligned} \tag{90}$$

Appendix B
Extraction of Winding Loss Model From FEM Simulations

Two-dimensional axisymmetric simulations were performed with the Tx and Rx coils driven by current sources. Although in practice, litz wire is typical, solid wire was used in these analyses as worst-case examples. The Tx coil currents were chosen to be the maximum current for each power class, and the Rx coil currents were selected to satisfy the maximum power level for the class, both specified in [35]. Winding losses can be determined from terminal measurements using different setups, where the effective resistances and geometric factors can be obtained as follows.

(a) *R_T and R_R*: The effective winding resistance R_{T} of the Tx coil can be calculated when the Rx coil is removed. The input power P_{Tx} is $\mathrm{Re}\{I_T^* I_T\} R_T$, which is the ohmic loss in the Tx coil. The winding resistance R_T can through the current I_T. Similarly, the winding resistance R_{R} of the Rx coil can also be calculated when the Tx coil is removed.

(b) *$R_{T:r}$, $R_{R:t}$: $R_{T:r}$, and $R_{R:t}$* can be calculated when one coil is open-circuited, while the other coil is driven. If the Tx coil is driven by I_T and the Rx coil is open-circuited ($I_R = 0$), the eddy current loss in the Rx coil $P_{\mathrm{Loss,eddy(Rx)}}$ can be derived from (17) resulting in

$$P_{\mathrm{Loss,eddy(Rx)}} = P_{\mathrm{Tx}} - \mathrm{Re}\{I_T^* I_T\} R_T. \tag{91}$$

Note that R_T was obtained previously; so $R_{T:r}$ can be calculated

$$R_{T:r} = \frac{P_{\mathrm{Loss,eddy(Rx)}}}{\mathrm{Re}\{I_T^* I_T\}}. \tag{92}$$

Similarly, $R_{R:t}$ can be obtained when the Rx is driven by I_R and the Tx coil is open-circuited ($I_T = 0$)

$$R_{R:t} = \frac{P_{\mathrm{Loss,eddy(Tx)}}}{\mathrm{Re}\{I_R^* I_R\}}. \tag{93}$$

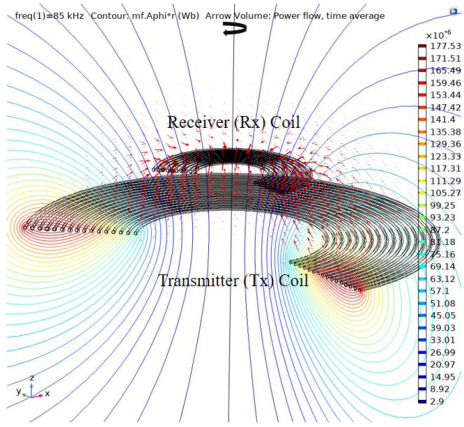

Fig. 41. Multiturn concentric solid wires were used for the Tx and Rx coils to emulate WPT2/Z1 class.

c) γ_T, γ_R: γ_T, and γ_R can be obtained when both the Tx and Rx currents are in phase, resulting in zero principal transfer-power ($P_{\mathrm{Tx:Rx}} = 0$), as discussed in Section II-B. $\gamma_{T,R}$ can be extracted from the the input and output power in (17) and (18)

$$\gamma_R = \frac{P_{\mathrm{Tx}} - \mathrm{Re}\{I_T^* I_T\} R_T - \mathrm{Re}\{I_T^* I_T\} R_{T:r}}{\mathrm{Re}\{I_T^* I_R\} R_T} \tag{94}$$

$$\gamma_T = \frac{P_{\mathrm{Rx}} - \mathrm{Re}\{I_R^* I_R\} R_R - \mathrm{Re}\{I_R^* I_R\} R_{R:t}}{\mathrm{Re}\{I_R^* I_T\} R_R}. \tag{95}$$

Table VI presents the coil specifications for different power and air gap classes. Fig. 41 shows an example with 7.7-kW output power when the Tx-to-Rx coil air gap is 100 mm, which emulates the WPT2/Z1 class; 2.5-mm radius[20] wire was used, where the Tx coil and Rx coil diameters were 650 and 250 mm, respectively.

Appendix C
Quadratic Approximation for the Mutual Inductance Over Lateral Misalignment

From Grover [37], the mutual inductance ($M_{T:R}$) of two coils consisting of circular filaments, which are laterally misaligned by x is

$$M_{T:R} = \frac{2\mu_0 \sqrt{r_T r_R}}{\pi} \int_0^{\pi} \frac{1 - \frac{x}{r_R}\cos\varphi}{k\sqrt{V^3}} \Psi(k)\, d\varphi \tag{96}$$

where

$$\alpha = \frac{r_R}{r_T},\ \beta = \frac{d_{T:R}}{r_T},\ V = \sqrt{1 + \frac{x^2}{r_R^2} - 2\frac{x}{r_R}\cos\varphi} \tag{97}$$

$$k^2 = \frac{4\alpha V}{(1+\alpha V)^2 + \beta^2},\ \Psi(k) = \left(1 - \frac{k^2}{2}\right) F(k) - E(k) \tag{98}$$

$$F(k) = \int_0^{\frac{\pi}{2}} \frac{d\theta}{\left(1 - k^2 \sin^2\theta\right)^{1/2}},$$

[20]The Tx and Rx wire radii were identically 2.5 mm for all classes, except for the Rx wire radii for the WPT1/Z1 (1.57 mm) and WPT1/Z2 (2.02 mm).

TABLE VI
LOSS BUDGET FOR VARIOUS WPT COIL CONFIGURATIONS (SOLID WIRE; SPIRAL WINDING): COIL SPECIFICATIONS

Power Class	Z-Class	r_T	r_R	$d_{T:R}$	N_T	N_R	I_T	I_R	R_T	R_R	$R_{T:r}$	$R_{R:t}$	$\gamma_R R_T = \gamma_T R_R$
WPT1	Z1	290	130.1	100	15	9+8 (2-layers)	30	10.6	0.36	0.58	0.022	6.8E-04	0.042
	Z2		159.2	140		20		12		0.63	0.038	4.6E-04	0.095
	Z3		210	170		20		9.9		0.31	0.015	1.3E-03	0.048
WPT2	Z1	325	125	100	16	10	75	23.3	0.18	0.074	0.016	2.0E-04	0.016
	Z2		160	140		9		17.7		0.065	8.1E-03	3.5E-04	0.01
	Z3		190	170		8		20		0.045	3.8E-03	3.0E-04	5.7E-03
WPT3	Z1	325	135	100	16	10	75	33.9	0.18	0.054	0.012	2.3E-04	0.011
	Z2		160	140		9		26.9		0.065	8.1E-03	3.5E-04	0.01
	Z3		190	170		8		30.4		0.045	3.8E-03	3.0E-04	5.7E-03

Table I and VI are FEM simulation results.
Power and Z-class are found in [35].
$r_{T,R}$ are the radii of the Tx and Rx coils. $d_{T:R}$ is the air gap between the Tx and Rx coils. The unit of the length is mm.
N_T and N_R are the number of turns for the Tx and Rx coils, respectively.
I_T and I_R are rms values. All the phase angle differences between the Tx and Rx coil currents are maintained at 90°.
The unit of the effective resistances R_T, R_R, $R_{T:r}$, $R_{R:t}$, $\gamma_R R_T$, and $\gamma_T R_R$ is Ohms (Ω).

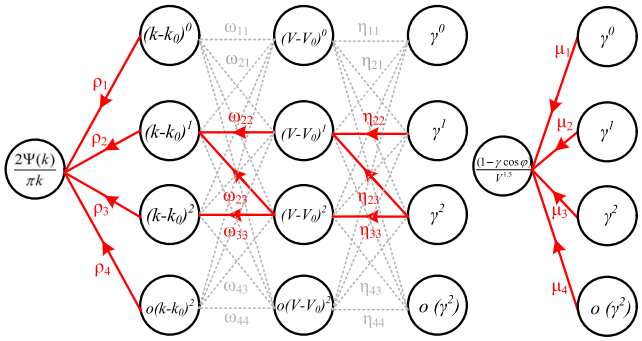

Fig. 42. Taylor expansion of the mutual inductance to the misalignment.

$$E(k) = \int_0^{\frac{\pi}{2}} \left(1 - k^2 \sin^2\theta\right)^{1/2} d\theta \tag{99}$$

r_T and r_R are the radii of the coils, $d_{T:R}$ is the vertical distance between two coils, x is the lateral misalignment, and k parameterizes the elliptic integrals.

We assume that the normalized misalignment $\gamma \triangleq x/r_R \ll 1$. This enables us to approximate the mutual inductance $M_{T:R}$ by a polynomial function of the normalized misalignment γ through Taylor expansion.

We first express $M_{T:R}$ as

$$M_{T:R} = \mu_0 \sqrt{r_T r_R} \int_0^{\pi} \underbrace{\left(1 - \frac{x}{r_R}\cos\varphi\right) V^{-\frac{3}{2}}}_{\text{A}} \times \underbrace{\frac{2\Psi(k)}{\pi k}}_{\text{B}} d\varphi. \tag{100}$$

The Taylor expansion of A in (100) can be expressed as

$$(1 - \gamma\cos\varphi)V^{-\frac{3}{2}} = \mu_1 + \mu_2\gamma + \mu_3\gamma^2 + o(\gamma^2) \tag{101}$$

where

$$\mu_1 = 1, \quad \mu_2 = \frac{1}{2}\cos\varphi, \quad \mu_3 = \frac{9}{8}\cos^2\varphi - \frac{3}{4}. \tag{102}$$

The Taylor expansion of B in (100) can be performed in three steps. The first step expands $2\Psi(k)/(\pi k)$ as a function of k, which is illustrated in the first layer of Fig. 42

$$\frac{2\Psi(k)}{\pi k} = \rho_1 + \rho_2(k - k_0) + \rho_3(k - k_0)^2 + o\left((k - k_0)^2\right) \tag{103}$$

where

$$\rho_1 = \frac{2 - k_0^2}{\pi k_0} F(k_0) - \frac{2}{\pi k_0} E(k_0) \tag{104}$$

$$\rho_2 = -\frac{2}{\pi k_0^2} F(k_0) + \frac{2 - k_0^2}{\pi(1 - k_0^2)k_0^2} E(k_0) \tag{105}$$

$$\rho_3 = \frac{(5k_0^4 - 9k_0^2 + 4)}{2\pi(k_0^2 - 1)^2 k_0^3} F(k_0) - \frac{(3k_0^4 - 9k_0^2 + 4)}{2\pi(k_0^2 - 1)^2 k_0^3} E(k_0) \tag{106}$$

$$k_0 = \sqrt{\frac{4\alpha}{(1+\alpha)^2 + \beta^2}}. \tag{107}$$

The following two equations are useful for deriving (103):

$$\frac{\mathrm{d}\,F(k)}{\mathrm{d}\,k} = \frac{E(k)}{k(1 - k^2)} - \frac{F(k)}{k} \tag{108}$$

$$\frac{\mathrm{d}\,E(k)}{\mathrm{d}\,k} = \frac{E(k) - F(k)}{k}. \tag{109}$$

The second step expands k as a function of V, which is illustrated in the second layer of Fig. 42

$$k = k_0 + \omega_{22}(V - V_0) + \omega_{23}(V - V_0)^2 + o\left((V - V_0)^2\right) \tag{110}$$

where

$$\omega_{22} = \frac{\alpha^{\frac{1}{2}}(1 - \alpha^2 + \beta^2)}{\left((1+\alpha)^2 + \beta^2\right)^{\frac{3}{2}}} \tag{111}$$

$$\omega_{23} = \frac{\alpha^{\frac{1}{2}}\left((1+\alpha)^2(3\alpha^2 - 6\alpha - 1) - 2\beta^2(5\alpha^2 + 4\alpha + 1) - \beta^4\right)}{4\left((1+\alpha)^2 + \beta^2\right)^{\frac{5}{2}}} \tag{112}$$

$$\omega_{33} = \omega_{22}^2 \tag{113}$$

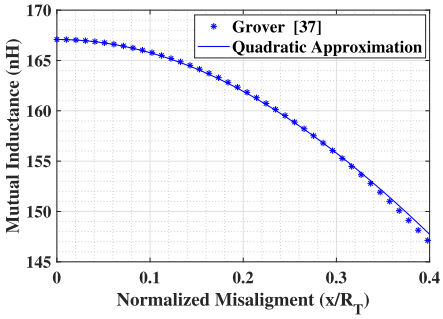

Fig. 43. Expression for the mutual inductance of circular filaments in Grover can be well approximated by a quadratic function when the misalignment distance is not too large relative to the radii of the coils.

$$V_0 = 1. \tag{114}$$

The third step expands V as a function of γ, which is illustrated in the third layer of Fig. 42.

$$V = V_0 + \eta_{22}\gamma + \eta_{23}\gamma^2 + o\left(\gamma^2\right) \tag{115}$$

where

$$\eta_{22} = -\cos\varphi \tag{116}$$

$$\eta_{23} = \frac{1}{2}\sin^2\varphi \tag{117}$$

$$\eta_{33} = \eta_{22}^2. \tag{118}$$

Through Fig. 42, the Taylor expansion of B in (100) is

$$\frac{2\Psi(k)}{\pi k} = \rho_1 + \rho_2\omega_{22}\eta_{22}\,\gamma + (\rho_2\omega_{22}\eta_{23} + \\ + \rho_2\omega_{23}\eta_{33} + \rho_3\omega_{33}\eta_{33})\,\gamma^2 + o\left(\gamma^2\right). \tag{119}$$

From (100), (101), and (119), we can extract the function that is a quadratic approximation $M_{T:R}$. Fig. 43 shows that the expression for mutual inductance in Grover can be well approximated by a quadratic function.

Appendix D
Derivation of FC-TPM for Lossy Coils

The Tx, Rx, and eddy winding currents in (63) can be expressed as

$$\begin{pmatrix} I_T \\ I_R \\ I_t \\ I_r \end{pmatrix} = \frac{1}{\mathcal{D}}\frac{1}{j\omega}\begin{pmatrix} W_{T:1} & W_{R:1} & W_{t:1} & W_{r:1} \\ W_{T:2} & W_{R:2} & W_{t:2} & W_{r:2} \\ W_{T:3} & W_{R:3} & W_{t:3} & W_{r:3} \\ W_{T:4} & W_{R:4} & W_{t:4} & W_{r:4} \end{pmatrix}\begin{pmatrix} V_1 \\ V_2 \\ V_3 \\ V_4 \end{pmatrix} \tag{120}$$

where $\mathcal{D}$ is the determinant and $W_{x:i}$ are the elements of the adjugate matrix of the mutual inductance matrix in (63).

For four sense coils, the transfer-power, decomposed into three power flows in (64), can be represented by three independent linear combinations of pairwise-products of sense coil voltages

$$\begin{aligned} P_{\text{Transfer}} &= P_{\text{Tx:Rx}} + P_{\text{Loss,eddy(Rx)}} - P_{\text{Loss,eddy(Tx)}} \\ &= \text{Re}\left\{j\omega M_{R:T} I_R I_T^*\right\} \\ &\quad + \text{Re}\left\{j\omega M_{T:r} I_r I_T^*\right\} - \text{Re}\left\{j\omega M_{R:t} I_t I_R^*\right\} \\ &= \sum_{i,j\in Q} \mathcal{A}_{ij}\left\langle V_i, V_j\right\rangle \\ &\quad + \sum_{i,j\in Q} \mathcal{B}_{ij}\left\langle V_i, V_j\right\rangle + \sum_{i,j\in Q} \mathcal{C}_{ij}\left\langle V_i, V_j\right\rangle \end{aligned} \tag{121}$$

where

$$\begin{bmatrix} \mathcal{A}_{12} \\ \mathcal{A}_{13} \\ \mathcal{A}_{14} \\ \mathcal{A}_{23} \\ \mathcal{A}_{24} \\ \mathcal{A}_{34} \end{bmatrix} = \frac{M_{R:T}}{\omega\mathcal{D}^2}\begin{bmatrix} W_{T:1}W_{R:2} - W_{T:2}W_{R:1} \\ W_{T:1}W_{t:2} - W_{T:2}W_{t:1} \\ W_{T:1}W_{r:2} - W_{T:2}W_{r:1} \\ W_{R:1}W_{t:2} - W_{R:2}W_{t:1} \\ W_{R:1}W_{r:2} - W_{R:2}W_{r:1} \\ W_{t:1}W_{r:2} - W_{t:2}W_{r:1} \end{bmatrix} \tag{122}$$

$$\begin{bmatrix} \mathcal{B}_{12} \\ \mathcal{B}_{13} \\ \mathcal{B}_{14} \\ \mathcal{B}_{23} \\ \mathcal{B}_{24} \\ \mathcal{B}_{34} \end{bmatrix} = \frac{M_{T:r}}{\omega\mathcal{D}^2}\begin{bmatrix} W_{T:1}W_{R:4} - W_{T:4}W_{R:1} \\ W_{T:1}W_{t:4} - W_{T:4}W_{t:1} \\ W_{T:1}W_{r:4} - W_{T:4}W_{r:1} \\ W_{R:1}W_{t:4} - W_{R:4}W_{t:1} \\ W_{R:1}W_{r:4} - W_{R:4}W_{r:1} \\ W_{t:1}W_{r:4} - W_{t:4}W_{r:1} \end{bmatrix} \tag{123}$$

$$\begin{bmatrix} \mathcal{C}_{12} \\ \mathcal{C}_{13} \\ \mathcal{C}_{14} \\ \mathcal{C}_{23} \\ \mathcal{C}_{24} \\ \mathcal{C}_{34} \end{bmatrix} = -\frac{M_{R:t}}{\omega\mathcal{D}^2}\begin{bmatrix} W_{T:2}W_{R:3} - W_{T:3}W_{R:2} \\ W_{T:2}W_{t:3} - W_{T:3}W_{t:2} \\ W_{T:2}W_{r:3} - W_{T:3}W_{r:2} \\ W_{R:2}W_{t:3} - W_{R:3}W_{t:2} \\ W_{R:2}W_{r:3} - W_{R:3}W_{r:2} \\ W_{t:2}W_{r:3} - W_{t:3}W_{r:2} \end{bmatrix}. \tag{124}$$

The transfer-power can thus be represented as a linear combination of pairwise-products of sense coil voltages in (65)

$$P_{\text{Transfer}} = \sum_{i,j\in Q} \lambda_{ij}\left\langle V_i, V_j\right\rangle \tag{125}$$

where

$$\lambda_{ij} = \mathcal{A}_{ij} + \mathcal{B}_{ij} + \mathcal{C}_{ij}. \tag{126}$$

If there are more than four sense coils, we can choose four sense coil voltages at a time from the total of N sense coils, from which a total of ${}^{N}\text{C}_4$ different formulations of (125) are constructed to determine the transfer-power. The transfer-power, therefore, can be determined by (65) for $N > 4$ sense coils, when all the formulations are summed and divided by $N_w = {}^{N}\text{C}_4$, resulting in a linear combination of the all pairwise-product of two sense coil voltages out of N sense coils

$$P_{\text{Transfer}} = \frac{1}{N_w}\sum_{k=1}^{N_w}\sum_{\substack{i<j \\ i,j\in s_k}} \lambda_{ij}^{(k)}\left\langle V_i, V_j\right\rangle \tag{127}$$

$$= \sum_{i,j \in Q} \zeta_{ij} \langle V_i, V_j \rangle \tag{128}$$

where

$$Q = \left\{ (i,j) \in \mathbb{N}^2 \,\middle|\, i \le N, j \le N, \text{ and } i < j \right\} \tag{129}$$

$$\zeta_{ij} = \frac{1}{N_w} \sum_{k \in \mathcal{G}_{ij}} {\lambda_{ij}}^{(k)} \tag{130}$$

$$\mathcal{G}_{ij} = \left\{ \mathcal{K} \subset \{1, \ldots, N_w\} \,\middle|\, k \in \mathcal{K} \text{ and } i, j \in s_k \right\} \tag{131}$$

$$\mathcal{S} = \{ s_k | \, s_k \subset \mathcal{T}, \ \mathrm{n}(s_k) = 4 \}. \tag{132}$$

Note that when $\mathcal{T}$ is a set of N sense coils, $\mathcal{T} = \{1, 2, \ldots, N\}$, $\mathcal{S}$ is a collection with lexical ordering of all subsets of $\mathcal{T}$ that consists of combinations of four sense coils, where $\mathrm{n}(\mathcal{S}) = N_w$.

APPENDIX E
REFERENCE STANDARD TRANSFER-POWER FOR THE CALIBRATION OF FC-TPM

Geometric constants that relate the sense coils' voltages to transfer-power need to be calibrated accurately. FC-TPM requires its geometric parameters α_{ij} from (52) to be calibrated for metering. As shown from (53) to (57), transfer-power should be known for the calibration of α_{ij}; an independent measurement of transfer-power is needed for the reference standard transfer-power.

Equation (12) shows that principal transfer-power is determined by the mutual reactance $\omega M_{T:R}$ from the Tx coil to the Rx coil, and the Tx and Rx coil currents I_T, I_R. We decompose the mutual reactance $\omega M_{R:T}$ to 1) the standard mutual reactance $\omega \check{M}_{R:T}$ that can be measured by only using magnitude of the open-circuited Rx coil voltage V_R and Tx coil current I_T, and 2) $\gamma_T R_R$, which accounts for the electromagnetic coupling from the Tx coil current to the Rx coil, as presented in Section III-A2. The transfer-power is then

$$P_{\text{Transfer}} = \mathrm{Re}\left\{ j\omega M_{R:T} I_R I_T^* \right\} \tag{133}$$

$$= \mathrm{Re}\left\{ j\sqrt{(\omega \check{M}_{R:T})^2 - (\gamma_T R_R)^2}\, I_R I_T^* \right\} \tag{134}$$

where $\omega M_{R:T}$ is derived from the open-circuited Rx coil voltage V_R, which can be derived from (90) in Appendix A with zero Rx coil current

$$\omega M_{R:T} = \frac{V_R}{j I_T} + j\gamma_T R_R \tag{135}$$

and the reference standard mutual reactance $\omega \check{M}_{R:T}$ is defined as the magnitude of ratio of the V_R to the I_T

$$\omega \check{M}_{R:T} \triangleq \left| \frac{V_R}{j I_T} \right|. \tag{136}$$

The reference standard transfer-power $\check{P}_{\text{Transfer}}$ is then defined by $\omega \check{M}_{R:T}$

$$\check{P}_{\text{Transfer}} \triangleq \mathrm{Re}\left\{ j\omega \check{M}_{R:T} I_R I_T^* \right\}. \tag{137}$$

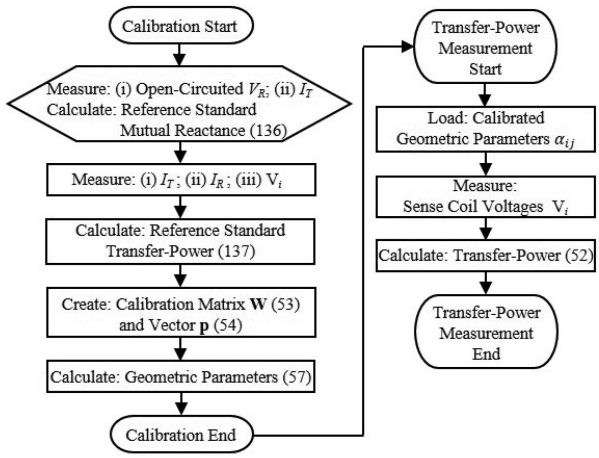

Fig. 44. Flowchart for calibration and subsequent transfer-power measurement with corresponding equation references.

Note that when $\gamma_T R_R$ is negligible ($\gamma_T R_R \ll \omega M_{R:T}$), the true transfer-power P_{Transfer} in (133) is accurately approximated by $\check{P}_{\text{Transfer}}$, where the percentage error ϵ_M is

$$\epsilon_M = \left| \frac{\check{P}_{\text{Transfer}} - P_{\text{Transfer}}}{P_{\text{Transfer}}} \right| \times 100\,(\%)$$

$$= \left| \sqrt{\left(1 + \left(\frac{\gamma_T R_R}{\omega M_{R:T}}\right)^2} - 1 \right| \times 100\,(\%). \tag{138}$$

The error ϵ_M is particularly small especially for the typically loosely coupled air-core WPT coils that have negligible $\gamma_T R_R$.

2-D axisymmetric FEM simulations were performed to verify the negligible error ϵ_M of reference standard transfer-power for WPT coils, which was used in the hardware demonstration. Fig. 44 illustrates the flow chart for calibration and subsequent transfer-power measurement. As a worst-case simulation, 2.5-mm diameter solid copper wires were used to make 45-cm diameter single-turn circular coils; ten of these circular coils were stacked to emulate the solenoidal Tx and Rx coils, where the solenoids' center-to-center air gap was 20 cm. The error ϵ_M is only $6.7 \times 10^{-7}\%$ when $\omega M_{R:T}$ is 6.967 Ω.

REFERENCES

[1] J. Huh, S. W. Lee, W. Y. Lee, G. H. Cho, and C. T. Rim, "Narrow-width inductive power transfer system for online electrical vehicles," *IEEE Trans. Power Electron.*, vol. 26, no. 12, pp. 3666–3679, Dec. 2011.

[2] G. A. Covic and J. T. Boys, "Inductive power transfer," *Proc. IEEE*, vol. 101, no. 6, pp. 1276–1289, Jun. 2013.

[3] S. Y. Choi, B. W. Gu, S. Y. Jeong, and C. T. Rim, "Advances in wireless power transfer systems for roadway-powered electric vehicles," *IEEE Trans. Emerg. Sel. Topics Power Electron.*, vol. 3, no. 1, pp. 18–36, Mar. 2015.

[4] C. C. Mi, G. Buja, S. Y. Choi, and C. T. Rim, "Modern advances in wireless power transfer systems for roadway powered electric vehicles," *IEEE Trans. Ind. Electron.*, vol. 63, no. 10, pp. 6533–6545, Oct. 2016.

[5] S. Li and C. C. Mi, "Wireless power transfer for electric vehicle applications," *IEEE Trans. Emerg. Sel. Topics Power Electron.*, vol. 3, no. 1, pp. 4–17, Mar. 2015.

[6] A. Daga, J. M. Miller, B. R. Long, R. Kacergis, P. Schrafel, and J. Wolgemuth, "Electric fuel pumps for wireless power transfer: Enabling rapid growth in the electric vehicle market," *IEEE Power Electron. Mag.*, vol. 4, no. 2, pp. 24–35, Jun. 2017.

[7] C. Wang, O. H. Stielau, and G. A. Covic, "Design considerations for a contactless electric vehicle battery charger," *IEEE Trans. Ind. Electron.*, vol. 52, no. 5, pp. 1308–1314, Oct. 2005.

[8] M. Pinuela, D. C. Yates, S. Lucyszyn, and P. D. Mitcheson, "Maximizing DC-to-load efficiency for inductive power transfer," *IEEE Trans. Power Electron.*, vol. 28, no. 5, pp. 2437–2447, May 2013.

[9] S. Y. R. Hui, W. Zhong, and C. K. Lee, "A critical review of recent progress in mid-range wireless power transfer," *IEEE Trans. Power Electron.*, vol. 29, no. 9, pp. 4500–4511, Sep. 2014.

[10] W. Zhang and C. C. Mi, "Compensation topologies of high-power wireless power transfer systems," *IEEE Trans. Veh. Technol.*, vol. 65, no. 6, pp. 4768–4778, Jun. 2016.

[11] T. Kan, T. Nguyen, J. C. White, R. K. Malhan, and C. C. Mi, "A new integration method for an electric vehicle wireless charging system using LCC compensation topology: Analysis and design," *IEEE Trans. Power Electron.*, vol. 32, no. 2, pp. 1638–1650, Feb. 2017.

[12] W. X. Zhong and S. Y. R. Hui, "Maximum energy efficiency tracking for wireless power transfer systems," *IEEE Trans. Power Electron.*, vol. 30, no. 7, pp. 4025–4034, Jul. 2015.

[13] M. Budhia, G. A. Covic, and J. T. Boys, "Design and optimization of circular magnetic structures for lumped inductive power transfer systems," *IEEE Trans. Power Electron.*, vol. 26, no. 11, pp. 3096–3108, Nov. 2011.

[14] R. Bosshard, J. W. Kolar, J. Mühlethaler, I. Stevanović, B. Wunsch, and F. Canales, "Modeling and η-α-Pareto optimization of inductive power transfer coils for electric vehicles," *IEEE Trans. Emerg. Sel. Topics Power Electron.*, vol. 3, no. 1, pp. 50–64, Mar. 2015.

[15] C. R. Sullivan and L. Beghou, "Design methodology for a high-Q self-resonant coil for medical and wireless-power applications," in *Proc. IEEE 14th Workshop Control Model. Power Electron.*, Jun. 2013, pp. 1–8, doi: 10.1109/COMPEL.2013.6626460.

[16] L. Percebon, D. Kuerschner, and S. Mathar, "Characterisation of factors influencing the magnetic leakage field of a 7 kW wireless electric vehicle charging system," in *Proc. IEEE PELS Workshop Emerg. Technol., Wireless Power Transfer*, Oct. 2016, pp. 145–151.

[17] J. Kim *et al.*, "Coil design and shielding methods for a magnetic resonant wireless power transfer system," *Proc. IEEE*, vol. 101, no. 6, pp. 1332–1342, Jun. 2013.

[18] "Global EV outlook 2019: Scaling-up the transition to electric mobility," *Int. Energy Agency, Paris, France*, Tech. Rep., May 2019.

[19] T. Covert, M. Greenstone, and C. R. Knittel, "Will we ever stop using fossil fuels?" *J. Econ. Perspectives*, vol. 30, pp. 117–38, Feb. 2016.

[20] "Electric power annual2018," *U.S. Energy Inf. Admin.*, Washington, DC, USA, Oct.2019.

[21] R. Cherif, F. Hasanov, and A. Pande, "Riding the energy transition: Oil beyond 2040," *IMF*, Washington, DC, USA,, Working Paper No. 17/120, May 2017.

[22] T. Bohn, "Scalable electric submeter challenges for electric vehicle charging; low level AC to DC extreme fast charging for commercial vehicles," in *Proc. IEEE Transp. Electrific. Conf. Expo*, Jun. 2019, pp. 1–9, doi: 10.1109/ITEC.2019.8790583.

[23] T. Minami, I. Tabuchi, R. Tanaka, and Y. Tsuruda, "Development of a real-time power and impedance sensor for wireless power transfer systems," in *Proc. IEEE Wireless Power Transfer Conf.*, May 2015, pp. 1–3, doi: 10.1109/WPT.2015.7140137.

[24] M. Zucca *et al.*, "Metrology for inductive charging of electric vehicles (MICEV)," in *Proc. AEIT Int. Conf. Elect. Electron. Technol. Automot.*, 2019, pp. 1–6, doi: 10.23919/EETA.2019.8804498.

[25] J. H. Spreen, "Electrical terminal representation of conductor loss in transformers," *IEEE Trans. Power Electron.*, vol. 5, no. 4, pp. 424–429, Oct. 1990.

[26] D. R. Zimmanck and C. R. Sullivan, "Efficient calculation of winding-loss resistance matrices for magnetic components," in *Proc. IEEE 12th Workshop Control Model. Power Electron.*, Jun. 2010, pp. 1–5, doi: 10.1109/COMPEL.2010.5562359.

[27] S. Y. Chu and A. Avestruz, "Transfer-power measurement: A non-contact method for fair and accurate metering of wireless power transfer in electric vehicles," in *Proc. IEEE 18th Workshop Control Model. Power Electron.*, Jul. 2017, pp. 1–8, doi: 10.1109/COMPEL.2017.8013344.

[28] S. Y. Chu, X. Cui, and A. Avestruz, "Accurate transfer-power measurement for wireless charging of electric vehicles under misalignment," in *Proc. IEEE PELS Workshop Emerg. Technol.: Wireless Power Transfer*, Jun. 2018, pp. 1–6, doi: 10.1109/WoW.2018.8450889.

[29] J. Kong, *Electromagnetic Wave Theory*. Hoboken, NJ, USA: Wiley, 1986.

[30] Y. Guo *et al.*, "Poynting vector analysis for wireless power transfer between magnetically coupled coils with different loads," *Sci. Rep.*, vol. 7, 2017, Art. no. 741.

[31] D. Cheng, *Field and Wave Electromagnetics (Addison-Wesley Series in Electrical Engineering)*. Reading, MA, USA: Addison-Wesley, 1989.

[32] Y. Liu and A. P. Hu, "Study of power flow in an IPT system based on poynting vector analysis," *Energies*, vol. 11, no. 1, 2018, Art. no. 165.

[33] D. Vyroubal, "Impedance of the eddy-current displacement probe: The transformer model," *IEEE Trans. Instrum. Meas.*, vol. 53, no. 2, pp. 384–391, Apr. 2004.

[34] J. García-Martín, J. Gómez-Gil, and E. Vázquez-Sánchez, "Non-destructive techniques based on eddy current testing," *Sensors*, vol. 11, no. 3, pp. 2525–2565, 2011.

[35] *Wireless Power Transfer for Light-Duty Plug-In/ Electric Vehicles and Alignment Methodology*, SAE J2954, SAE, Warrendale, PA, USA, May 2016.

[36] A. V. Oppenheim and R. W. Schafer, *Discrete-Time Signal Processing*. 3rd ed. Upper Saddle River, NJ, USA: Prentice Hall Press, 2009.

[37] F. Grover, *Inductance Calculations* (Dover Books on Electrical Engineering). Mineola, NY, USA: Dover, 2013.

[38] S. Babic, F. Sirois, C. Akyel, and C. Girardi, "Mutual inductance calculation between circular filaments arbitrarily positioned in space: Alternative to Grover's formula," *IEEE Trans. Magn.*, vol. 46, no. 9, pp. 3591–3600, Sep. 2010.

[39] A. C. Cameron and F. A. Windmeijer, "An R-squared measure of goodness of fit for some common nonlinear regression models," *J. Econometrics*, vol. 77, no. 2, pp. 329–342, 1997.

[40] K. P. Murphy, *Machine Learning: A Probabilistic Perspective*. Cambridge, MA, USA: MIT Press, 2012.

[41] G. L. Harris and L. Eason, "Specifications and tolerances for reference standards and field standard weights and measures, 3. Specifications and tolerances for graduated neck type volumetric field standards," Nat. Inst. Standards Technol., Gaithersburg, MD, USA, *NIST HB-105-3 2009*, Feb. 2010.

[42] G. L. Harris and V. R. Miller, "Selected procedures for volumetric calibrations," Nat. Inst. Standards Technol., Gaithersburg, MD, USA, NIST Interagency/Intern. Rep. 7383, May 2019.

[43] X. Nan and C. R. Sullivan, "An equivalent complex permeability model for litz-wire windings," *IEEE Trans. Ind. Appl.*, vol. 45, no. 2, pp. 854–860, Mar./Apr. 2009.

[44] A. Delgado, G. Salinas, J. A. Oliver, J. A. Cobos, and J. Rodriguez-Moreno, "Equivalent conductor layer for fast 3-D finite element simulations of inductive power transfer coils," *IEEE Trans. Power Electron.*, vol. 35, no. 6, pp. 6221–6230, Jun. 2020.

[45] A. Stadler and C. Gulden, "Copper losses of litz-wire windings due to an air gap," in *Proc. 15th Eur. Conf. Power Electron. Appl.*, 2013, pp. 1–7, doi: 10.1109/EPE.2013.6631820.

[46] S. Y. Chu, X. Zan, and A. -T. Avestruz, "Electromagnetic Model-Based Foreign Object Detection for Wireless Power Transfer," *IEEE Trans. Power Electron.*, vol. 37, no. 1, pp. 100–113, Jan. 2022, doi: 10.1109/TPEL.2021.3100420.

[47] S. Boyd and L. Vandenberghe, *Convex Optimization*. New York, NY, USA: Cambridge Univ. Press, 2004.

[48] D. P. Bertsekas, *Constrained Optimization and Lagrange Multiplier Methods*. New York, NY, USA: Academic, 2014.

[49] M. A. Prelee and D. L. Neuhoff, "Multidimensional Manhattan sampling and reconstruction," *IEEE Trans. Inf. Theory*, vol. 62, no. 5, pp. 2772–2787, May 2016.

[50] H. W. Ott, *Noise Reduction Techniques in Electronic Systems*, 2nd ed. New York, NY, USA: Wiley, 1988.

[51] X. Zan and A. Avestruz, "27.12 MHz bi-directional wireless power transfer using current-mode class D converters with phase-shift power modulation," in *Proc. IEEE PELS Workshop Emerg. Technol., Wireless Power Transfer*, Jun. 2018.

[52] X. Zan and A. Avestruz, "Performance comparisons of synchronous and uncontrolled rectifiers for 27.12 MHz wireless power transfer using CMCD converters," in *Proc. IEEE Energy Convers. Congr. Expo.*, Sep. 2018, pp. 2448–2455.

[53] X. Zan, Z. Guo, and A. Avestruz, "Inductive wireless power transfer at 100 MHz with wide load range and constant output current," in *Proc. IEEE Energy Convers. Congr. Expo.*, Sep. 2019, pp. 4967–4975.

[54] R. Muñiz, J. Díaz, F. Nuño, M. J. Prieto, and A. M. Pernía, "A smart power meter to recharge electric vehicles in communal parking areas," *IEEE Internet Things J.*, vol. 6, no. 2, pp. 3448–3454, Apr. 2019.
[55] A. Muharam, M. Pratama, K. Ismail, S. Kaleg, M. R. Kurnia, and A. Hapid, "A development of smart metering infrastructure for electric vehicle charging point," in *Proc. Int. Conf. Sustain. Energy Eng. Appl.*, 2016, pp. 27–33.
[56] L. Qiao, X. Liu, and B. Jiang, "Design and implementation of the smart meter in vehicle-to-grid," in *Proc. 4th Int. Conf. Electr. Utility Deregulation Restruct. Power Technol.*, 2011, pp. 618–621.
[57] T. Butcher, L. Crown, and R. Harshman, *NIST Handbook 44: Specifications, Tolerances, and Other Technical Requirements for Weighing and Measuring Devices*. Gaithersburg, MD, USA: Nat. Inst. Standards Technol., 2017.

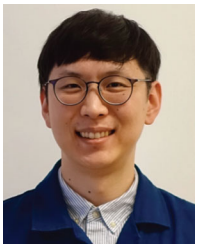

Sung Yul Chu (Student Member, IEEE) received the B.S. and M.S. degrees in electrical and electronic engineering from Yonsei University, Seoul, South Korea, in 2009 and 2011, respectively. He is currently working toward the Ph.D. degree in electrical and computer engineering with the University of Michigan, Ann Arbor, MI, USA.

In 2013, he was an Assistant Hardware Engineer with Samsung Electronics, Suwon, South Korea. From 2014 to 2016, he was a Junior Research Engineer with Hyundai Kefico (Hyundai Motor Group), Gunpo, South Korea. He was selected as a finalist for the 2020 Lemelson-MIT "Move it!" Graduate Student Prize in recognition of the invention of *Transfer-Power Measurement* for fair metering of wireless charging in electric vehicles. His research interests include power electronics, wireless power transfer, electromagnetic modeling, sensing and detection applications for energy, automotive, and consumer electronics.

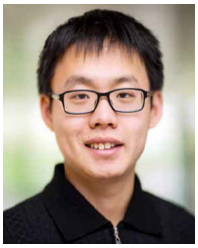

Xiaofan Cui (Student Member, IEEE) received the B.S. degree in electrical engineering and automation from Tsinghua University, Beijing, China, in 2016. He is currently working toward the Ph.D. degree in electrical and computer engineering with the University of Michigan, Ann Arbor, MI, USA.

He was a Visiting Student with Stanford University, Stanford, CA, USA, during the summer of 2015. His research interests include the modeling, digital control, and design of high-performance power electronics and energy systems.

Mr. Cui was the recipient of Richard F. and Eleanor A. Towner Prize for Distinguished Academic Achievement in ECE at the University of Michigan in 2021.

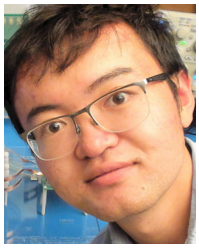

Xin Zan (Student Member, IEEE) received the B.E. degree in electrical engineering and automation from Tsinghua University, Beijing, China, in 2016. He is currently working toward the Ph.D. degree in electrical and computer engineering with the University of Michigan, Ann Arbor, MI, USA.

His research research interests include high-frequency and very high-frequency power electronics and pulse electronics.

Mr. Zan was the recipient of IEEE Power Electronics Society (PELS) ECCE Best Student Project Demonstration on Emerging Technology 2nd Prize Award, in 2018, IEEE PELS Best ECCE Paper on Emerging Technology Award Oral Presentation, in 2019, the Richard F. and Eleanor A. Towner Prize for Distinguished Academic Achievement from the University of Michigan, in 2019, and Rackham Predoctoral Fellowship from the University of Michigan, in 2021.

Al-Thaddeus Avestruz (Member, IEEE) received the SB in physics with electrical engineering, the SM and EE degrees, and the Ph.D. degree in electrical engineering and computer science from the Massachusetts Institute of Technology, Cambridge, MA, USA, in 2006 and 2016, respectively.

He is currently an Assistant Professor of electrical and computer engineering with the University of Michigan, Ann Arbor, MI, USA. He has over a decade of industry and entrepreneurial experience, and holds ten issued U.S. patents. His research interests include the design, modeling, and control of high-performance power electronics and wireless power transfer for energy, mobility, medicine, and the Internet of Things. He has complementary interests in circuits and systems for sensing, electromagnetic systems, feedback and controls, renewable energy, automotive, biomedical, and consumer applications.

Dr. Avestruz is a member of the IEEE Power Electronics Society, where he is the Chair of TC1: Technical Committee on the Control and Modeling of Power Electronics. He was the recipient of the IEEE PELS Best ECCE Paper on Emerging Technology Award Oral Presentation, in 2019. He is an Associate Editor for the IEEE OPEN JOURNAL OF POWER ELECTRONICS, a Guest Associate Editor for the IEEE JOURNAL OF EMERGING AND SELECTED TOPICS IN POWER ELECTRONICS, an Associate Technical Program Chair for the IEEE Energy Conversion Congress and Exposition, in 2019, a Technical Program Co-Chair for the 2021 IEEE Wireless Power Week, General Chair for the 24th IEEE Workshop on Control and Modeling for Power Electronics in 2023.